Recent progress in understanding electron thermal transport in NSTX

You may also be interested in:

Chapter 2: Plasma confinement and transport
E.J. Doyle (Chair Transport Physics), W.A. Houlberg (Chair Confinement Database and Modelling), Y. Kamada (Chair Pedestal and Edge) et al.

Overview of physics results from the conclusive operation of the National Spherical Torus Experiment
S.A. Sabbagh, J.-W. Ahn, J. Allain et al.

Electron-scale turbulence spectra and plasma thermal transport responding to continuous E × B shear ramp-up in a spherical tokamak
Y. Ren, W. Guttenfelder, S.M. Kaye et al.

Progress in simulating turbulent electron thermal transport in NSTX
W. Guttenfelder, J.L. Peterson, J. Candy et al.

An overview of recent physics results from NSTX
S.M. Kaye, T. Abrams, J.-W. Ahn et al.

Energetic particle physics in fusion research in preparation for burning plasma experiments
N.N. Gorelenkov, S.D. Pinches and K. Toi

Improved understanding of physics processes in pedestal structure, leading to improved predictive capability for ITER
R.J. Groebner, C.S. Chang, J.W. Hughes et al.

Reduced electron thermal transport in low collisionality H-mode plasmas in DIII-D and the importance of TEM/ETG-scale turbulence
L. Schmitz, C. Holland, T.L. Rhodes et al.

Recent progress in understanding electron thermal transport in NSTX

Y. Ren[1,a], E. Belova[1], N. Gorelenkov[1], W. Guttenfelder[1], S.M. Kaye[1], E. Mazzucato[1], J.L. Peterson[2], D.R. Smith[3], D. Stutman[4], K. Tritz[4], W.X. Wang[1], H. Yuh[5], R.E. Bell[1], C.W. Domier[6] and B.P. LeBlanc[1]

[1] Princeton Plasma Physics Laboratory, Princeton, NJ 08543, United States of America
[2] Lawrence Livermore National Laboratory, Livermore, CA 94551, United States of America
[3] University of Wisconsin-Madison, Madison, WI 53706, United States of America
[4] Johns Hopkins University, Baltimore, MD 21218, United States of America
[5] Nova Photonics, Inc., Princeton, NJ 08540, United States of America
[6] University of California at Davis, Davis, CA 95616, United States of America

E-mail: yren@pppl.gov

CrossMark

Abstract

The anomalous level of electron thermal transport inferred in magnetically confined configurations is one of the most challenging problems for the ultimate realization of fusion power using toroidal devices: tokamaks, spherical tori and stellarators. It is generally believed that plasma instabilities driven by the abundant free energy in fusion plasmas are responsible for the electron thermal transport. The National Spherical Torus eXperiment (NSTX) (Ono *et al* 2000 *Nucl. Fusion* **40** 557) provides a unique laboratory for studying plasma instabilities and their relation to electron thermal transport due to its low toroidal field, high plasma beta, low aspect ratio and large $E \times B$ flow shear. Recent findings on NSTX have shown that multiple instabilities are required to explain observed electron thermal transport, given the wide range of equilibrium parameters due to different operational scenarios and radial regions in fusion plasmas. Here we review the recent progresses in understanding anomalous electron thermal transport in NSTX and focus on mechanisms that could drive electron thermal transport in the core region. The synergy between experiment and theoretical/numerical modeling is essential to achieving these progresses. The plans for newly commissioned NSTX-Upgrade will also be discussed.

Keywords: electron thermal transport, spherical tokamak, NSTX, confinement and transport

(Some figures may appear in colour only in the online journal)

1. Introduction

Electron thermal transport will likely pose the ultimate limit to the confinement performance of future devices. For example, electron heating will be dominant in ITER discharges, and efficient heating of fuel ions by electrons requires good electron thermal confinement. Thus understanding the mechanism behind anomalous electron thermal transport is of great importance for predicting and optimizing confinement performance of future magnetic confinement devices, e.g. ITER and Fusion

nuclear science facility (FNSF) [1]. It is generally believed that plasmas instabilities driven unstable by free energy existing in fusion plasmas are responsible for the electron thermal transport [2, 3]. The turbulent sources of the electron transport can be on the short-wavelength electron scale or longer wavelength ion scales. Pure micro-instability modes in each regime include electron temperature gradient (ETG) modes in the short-wavelength regime ($k_\theta \rho_e \lesssim 1$) [4, 5], or ion temperature gradient (ITG) mode [6], trapped electron mode (TEM) [7], kinetic ballooning modes (KBMs) [8] or micro-tearing (MT) mode [9–11] at longer wavelengths ($k_\theta \rho_i \lesssim 1$), where k_θ is the poloidal wavenumber and ρ_e and ρ_i are the electron and

[a] Author to whom any correspondence should be addressed.
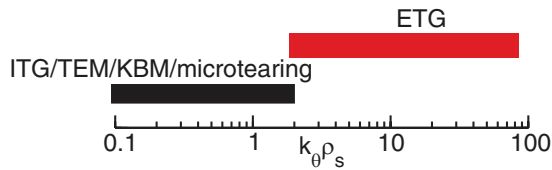
Figure 1. A schematic of typical wavenumber ranges for ion and electron-scale drift waves in NSTX, where ρ_s is the ion gyro-radius at electron temperature.

ion gyro-radii. A schematic of typical wavenumber ranges for different ion and electrons-scale drift waves can be seen in figure 1. Hybrids or combinations of the above modes or cascading of power from one wavelength regime to the other may also be important. In addition to micro-instabilities described above, macro-instabilities can also lead to electron thermal transport. In particular, high frequency Alfvén eigenmode (AE) activities were shown to be able to drive electron thermal transport [12, 13].

The National Spherical Torus eXperiment (NSTX) provides a unique laboratory for studying plasma instabilities and their relation to electron thermal transport. The low toroidal field of NSTX, approximately a factor of five lower than that in conventional aspect ratio devices, leads to plasma operations in parameter regimes that are different from those at higher aspect ratio and this provides new opportunities to make new diagnostic measurements and to extend and benchmark theory. The enhanced toroidicity and natural shaping at low aspect ratio is predicted to lead to reduced microturbulence levels in ion-scale range [14], and thus reduced ion-thermal transport associated with the microturbulence. Enhanced toroidicity also results in higher trapped particle fractions, which can influence trapped electron mode (TEM) turbulence and zonal flow damping. Furthermore, the low toroidal field and near Mach flow yield large values of the $E \times B$ shearing rate, believed to be important for the suppression of ion-scale micro-turbulence and its associated transport. Indeed, it is well established in NSTX that ion thermal transport could be reduced to neoclassical level in neutral beam injection (NBI)-heated H-mode plasmas [15]. On the other hand, electron thermal transport is consistently anomalous and almost always dominates in thermal transport. For example, figure 2(*a*) shows electron thermal diffusivity (χ_e), ion thermal diffusivity (χ_i) profiles derived from power balance analysis using TRANSP [16] together with neoclassical ion thermal diffusivity, $\chi_{i,\text{nc}}$, calculated with NCLASS model [17] for an NSTX NBI-heated H-mode plasma. Good agreement between measured χ_i and $\chi_{i,\text{nc}}$ is evident. We note that, on the other hand, ion thermal transport in NSTX L-mode plasmas can be significantly larger than neoclassical values (see [18, 19]). It is also clear that χ_e is much larger than χ_i and that electron thermal transport dominates the total heat loss from the plasma. It is interesting to point out that the χ_e values in NSTX can be in the range of 5–30 χ_e^{gyroBohm} ($\sim$30χ_e^{gyroBohm} location is denoted in figure 2(*a*)), which is what would be expected for ETG-driven electron thermal transport [20]. To further demonstrate the neoclassical level of ion thermal transport, a prediction of ion temperature, T_i, using the Chang–Hinton neoclassical

transport model was carried out using the TRANSP code [16] and good agreement with measured T_i can be readily seen in figure 2(*b*). Additionally, NSTX operates in regimes whose plasma collisionality is similar to that of conventional aspect ratio tokamaks, but in which plasma beta, β, and the electron and ion gyroradii (ρ_e, ρ_i respectively) can be up to a factor of 10 greater than those at higher toroidal field and aspect ratio. The high β (up to 40%) enables NSTX to explore electromagnetic and stochastic magnetic effects that may influence transport, and the large electron gyroradius ($\sim$0.1 mm) allows a direct measurement of spatially-resolved electron-scale turbulence.

Given all the possible mechanisms that may drive electron thermal transport, it is not surprising that a universal mechanism for explaining anomalous electron thermal transport in NSTX is not yet identified. In fact, there are good experimental indications that no single mechanism can explain observed electron thermal transport in NSTX. After all, there are different parameters regimes in which NSTX can operate and there are also different radial regions in the same plasma that have dramatically different equilibrium parameters, e.g. temperature and density gradients. For example, NSTX radio frequency (RF)-heated L-mode plasmas, which feature a large T_e/T_i ratio and large electron temperature gradient, were shown to be unstable to TEM and ETG instabilities [21], while NSTX NBI-heated L-mode plasmas with large $E \times B$ shear were shown to be unstable to ITG and ETG instabilities [19] and possibly also unstable to the Kevin–Helmholtz (KH) instability [22]. The large variation in equilibrium gradients, particularly those of electron density and temperature, from tokamak core to the edge also indicates the need of different mechanisms in different radial regions. Here, we use NSTX H-mode plasmas as example. Drift wave instabilities are typically very weak if not stable in the NSTX H-mode plasma center, named as the core flat region, due to small equilibrium gradients and thus mechanisms rather than microturbulence are needed to explain the flat electron temperature profiles [12, 13, 23]. Around mid-radius, i.e. $r/a \sim 0.5$ (r is the minor radius and a is the half width of the last closed flux surface at mid-plane), the equilibrium gradients become larger, and drift wave instabilities, e.g. ITG, TEM, MT and/or ETG, can be unstable and could drive electron thermal transport (this region is named as the core gradient region). The H-mode pedestal region is characterized by much larger gradients, higher collisionality, larger magnetic shear ($\hat{s}$) and safety factor (q), and lower plasma β than the core gradient region. This can drive different drift wave instabilities than in the core gradient region and on the other hand, some drift wave instabilities which were found in the the core gradient region also work in the edge, e.g. MT and ETG mode (see [24]). As an example, it was shown that while the MT modes are unstable without lithium at the pedestal top, they are stabilized by the stronger density gradient with lithium [24].

It is important to note that the recently commissioned NSTX-Upgrade (NSTX-U) [25] will be a more capable platform for our continued study of electron thermal transport. NSTX-U has doubled toroidal field, plasma current and NBI heating power, which allows it to reach new parameter regimes more relevant to future devices, such as lower
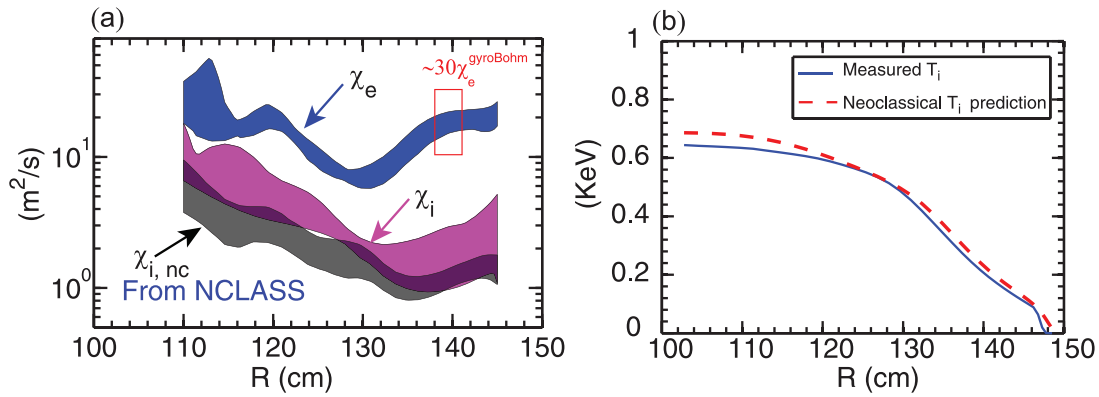
Figure 2. (*a*) Radial profiles of electron thermal diffusivity (χ_e), ion thermal diffusivity (χ_i) and neoclassical ion thermal diffusivity ($\chi_{i,\text{nc}}$, calculated with the NCLASS model) in an NSTX NBI-heated H-mode plasma (shot 141007), where χ_e can be about $30\chi_e^{\text{gyroBohm}}$ within the radial region denoted by the red rectangular; (*b*) Radial profiles of measured T_i and prediction of T_i using the TRANSP code with the Chang–Hinton neoclassical transport model for the same shot.

collisionality, and to have new control capabilities, e.g. modifying current and flow profiles. This upgrade makes it possible to make new turbulence measurements and to isolate/determine the regime of validity of a variety of instabilities in driving electron thermal transport. In addition, enhanced turbulence diagnostics measuring both large and small wavenumbers on NSTX-U will allow more detailed comparisons with nonlinear gyrokinetic simulations.

In this paper, we aim to provide a review of recent progress in understanding anomalous electron thermal transport in NSTX and will be focusing on the mechanisms that could drive electron thermal transport in the core region (mechanisms in the edge region, e.g. the H-mode pedestal region, is beyond the scope of this paper). We note that this progress is the results from the synergies between experimental measurements and theoretical/numerical modelings. We also note that we are not attempting to provide a comprehensive survey of possible instabilities that could drive electron thermal transport (we focus here rather on instabilities that have more substantial experimental and theoretical evidence) and a more complete summary of gyrokinetic studies of electron thermal transport in NSTX can be found in [26].

We would also like to emphasize that the mechanisms for anomalous electron thermal transport we reviewed in the paper, particularly the MT mode and ETG mode, are very relevant to conventional tokamaks. For example, MT mode has been found to be unstable at the pedestal top of conventional tokamaks [27, 28] and ETG modes may be important for DIII-D high beta poloidal plasmas featuring dominant neoclassical ion thermal transport and large anomalous electron thermal transport [29]. The results presented in this paper have given insight into questions that are relevant to both spherical tokamak and conventional tokamak: Can we experimentally identify these modes? Can we experimentally establish the correlation between the modes and electron thermal transport? Can these modes drive experimentally relevant electron thermal transport? How can we control these modes? Furthermore, since NSTX operate in a different parametric regime than the conventional tokamak, e.g. higher beta, lower

aspect and stronger $E \times B$ shear, the presented gyrokinetic simulations are also validation practices of the numerical codes in the unique spherical tokamak parametric regime in addition to the existing validation effort on conventional tokamaks.

The paper is organized as follows. In section 2, we will be focusing on mechanisms in the core gradient region. Two mechanisms, MT and ETG, will be discussed in detail in sections 2.1 and 2.2, respectively. In section 3, we will be focusing on the core flat region where mechanisms rather than microturbulence are needed to explain the flat temperature profiles [12, 13, 23]. Lastly, we will summarize and make discussions in section 4.

2. Electron thermal transport in the core gradient region

As we briefly discussed in section 1, the core gradient region has abundant free energy due to equilibrium gradients so that drift-wave-type micro-instabilities could be important for driving electron thermal transport. As presented in [26], all the drift wave instabilities discussed in section 1 could be unstable in NSTX and contribute to electron thermal transport. However, here we will be focusing on two leading candidates: micro-tearing mode and ETG mode which have the best experimental and numerical evidence for their roles in driving electron thermal transport in NSTX.

2.1. Micro-tearing Mode

One unique feature of ST confinement is that the global energy confinement has a strong inverse dependence on electron collisionality [15, 30–32]: $B\tau_E \sim 1/\nu_e^*$, while the ITER scaling on collisionality is much weaker: $B\tau_E \sim \nu_e^{*-0.01}$ [33]. The ST confinement scaling leads to an order magnitude of improvement in projected performance of ST-FNSF in contrast to that from the ITER scaling as shown in [25]. Furthermore, as seen in figure 3, this ST global energy confinement scaling
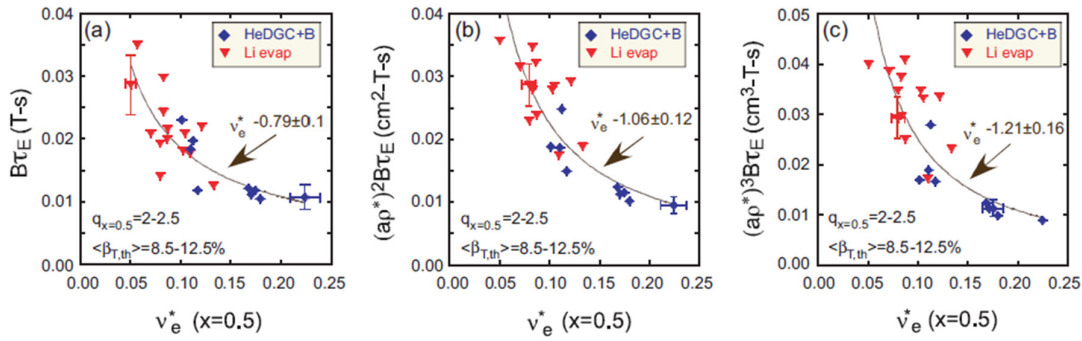
Figure 3. Normalized confinement time as a function of collisionality at $\rho = 0.5$ (ρ is the square root of normalized toroidal flux) for the ν_e^* scan for assuming (*a*) $B\tau_E \sim \rho^{*0}$, (*b*) Bohm scaling, $B\tau_E \sim \rho^{*-2}$ and (3) gyroBohm scaling, $B\tau_E \sim \rho^{*-3}$. Blue points are from discharges that used HeGDC + B wall conditioning, while red points are from discharges that used Li evap. Discharges from the above scans were constrained to have minimal variation in $q_{r/a=0.5}$ (2–2.5) and $\langle \beta_T \rangle$ (8.5–12.5%). Note that to account for the variation in ρ^*, scalings were also determined assuming either a Bohm ($B\tau_E \sim \rho^{*-2}$) or gyroBohm ($B\tau_E \sim \rho^{*-3}$) dependence. Stronger dependence with collisionality, $B\tau_E \sim \nu_e^{*-1.06}$ and $B\tau_E \sim \nu_e^{*-1.21}$, is found for Bohm and gyroBohm scaling assumptions. Reproduced courtesy of IAEA. Figure from [30]. Copyright (2013) IAEA.

is seen to be independent of wall conditioning, either using helium glow discharge cleaning plus occasional boronization for wall conditioning (HeGDC + B) or between-shot lithium conditioning of the vessel walls through evaporation from two LITERs (lithium evaporators) mounted at the top of the NSTX vessel [30]. This collisionality dependence also unifies the different engineering scaling observed with different wall condition: $\tau_{th} \sim I_p^{0.37} B_T^{1.01}$ for HeGDC + B wall conditioning and $\tau_{th} \sim I_p^{0.79} B_T^{-0.15}$ for lithium wall conditioning with the latter scaling similar to those in conventional aspect ratio tokamaks, as embodied in the ITER98$_{y,2}$ scaling [33] with a strong I_p dependence and a weak B_T dependence. This unification implies that collisionality is more fundamental in determining energy confinement and the difference in engineering scalings comes from how the engineering parameters are correlated with collisionality. Indeed, it is found that with HeGDC + B wall conditioning, reduction in electron collisionality is mostly correlated with the increase in B_T and on the other hand, when lithium is used for wall conditioning, the reduction in electron collisionality is correlated well with increase in amount of lithium deposition. An electron temperature profile broadening with decreasing collisionality is seen in both cases. On the other hand, ion thermal transport remains on the neoclassical level. This confinement scaling dependence on electron collisionality naturally motivated the searching for transport mechanisms that mainly drive electron thermal transport and have strong dependence on electron collisionality. The MT mode [9, 10, 34] is a natural candidate. It is driven unstable by electron temperature gradient and requires sufficient electron–ion collisions to be unstable. Since the MT mode drives electron thermal transport through field-line stochasticity from magnetic island overlapping, no ion thermal transport is expected due to the much slower ion thermal velocity and much larger ion gyro-radii. Furthermore, the MT mode is an electromagnetic mode and is expected to be much more important in STs, which have much higher plasma β than conventional tokamaks. Indeed, the MT mode was found

to be unstable with gyrokinetic linear stability analysis in many NSTX high ν_e^* H-mode plasmas and was also shown to generate experimentally relevant electron thermal transport from gyrokinetic simulations [11, 35, 36]. We will review this progress in simulating the MT mode in NSTX in this section.

One important indication of the potential importance of the MT mode is that it can be the dominant instability over a significant region of NSTX plasmas as shown in [35]. Figure 4 shows the real frequencies (figure 4(*a*)) and linear growth rates (figure 4(*b*)) from local linear micro-stability analysis of a high collisionality NSTX H-mode plasma at four radial locations, i.e. $r/a = 0.5, 0.6, 0.7, 0.8$. The MT mode is found to be dominant between $r/a = 0.5$–0.8 with real frequencies in the electron diamagnetic drift direction and growth rates peaking at about $k_\theta \rho_s = 0.6$–0.8 (translating to $n \approx 40$–50, where n is the toroidal mode number), except for the location of $r/a = 0.7$ where MTs are are unstable at even higher wavenumbers up to $k_\theta \rho_s \lesssim 5$. We note that this particular behavior of MT modes at $r/a = 0.7$ is most likely related to the magnetic shear ($\hat{s} = 3.26$) at this location (see figure 12(*b*) in [35] and related discussion for more details). The calculated real frequencies are in agreement with the electron diamagnetic drift frequency, consistent with theoretical expectation of the MT mode [9, 10]. The calculated mode structure of shear magnetic perturbation, $A_\parallel$, is strongly ballooning and symmetric around the outboard midplane (even parity), indicative of a tearing-mode-type magnetic field perturbation [35] and in agreement with that of the MT mode. The $E \times B$ shearing rate is found to be comparable to the MT maximum linear growth rate and nonlinear suppression of the MT turbulence may be important as initially found in [11]. It was also found that ETG instability at higher $k_\theta \rho_s$ is stable in this plasma and all drift wave modes are stable at $r/a < 0.45$, and thus the MT is likely playing an important role in determining the electron thermal transport. The situation becomes more complicated towards the edge of the plasma: a KBM branch starts to appear at $r/a = 0.8$ (see figure 4) with the MT mode dominating at around $k_\theta \rho_s = 0.5$–0.7 (the KBM branch was traced by the GYRO eigenvalue
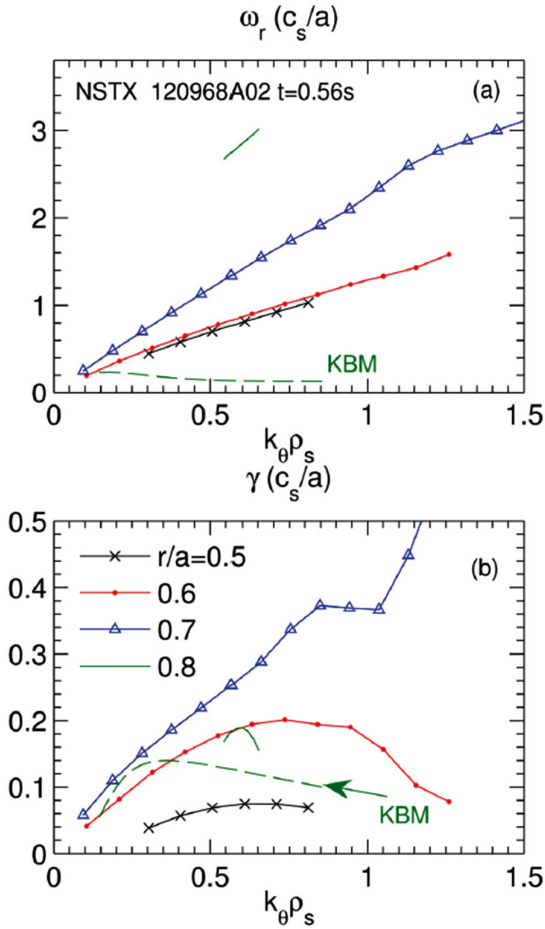
Figure 4. Real frequency and growth rate spectra for $r/a = 0.5$–0.8. Solid lines represent MT modes, while the dashed line represents KBMs calculated at $r/a = 0.8$ using eigenvalue solver. Linear gyrokinetic simulations were performed for a high collisionality NSTX H-mode plasma which is part of a dimensionless confinement scaling study (shot 120968 with $B_T = 0.35$ T, $I_p = 0.7$ MA, $R/a = 0.82/0.62$ m and $P_{NBI} = 4$ MW). Linear runs were conducted with GYRO gyrokinetic code [37], including kinetic electrons, deuterium ion and carbon impurity, full electromagnetic effects and electron pitch angle scattering. Equilibrium reconstruction used in the simulations is from LRDFIT [38]. Reproduced from [35], with the permission of AIP Publishing.

solver). This is not surprising since both the electron density and temperature gradients increase towards the edge, leading to large generalized MHD-α parameter [39] that drives KBMs.

A parametric scan in electron collisionality based on experimental equilibria reveals that the linear growth rate peaks at some finite electron collisionality, one of most distinguishing features of the MT mode, as shown in figure 5, where $\nu_{ei} = 4\pi n_e e^4 \log \Lambda/(2T_e)^{3/2} m_e^{1/2}$ and the electron–ion collision frequency is determined by $\nu^{e/i} = Z_{eff} \cdot \nu_{ei}$ (Z_{eff} is the effective ionic charge). Two scans in ν_{ei}, one with the experimental value of $Z_{eff} = 2.9$ and the other $Z_{eff} = 1$ (obtained by setting the carbon impurity content to be zero), are shown in figure 5 to clarify the dependence of linear growth rate on collisionality. Note that the $Z_{eff} = 1$ case has the peak linear growth rate at a ν_{ei} value larger than the ν_{ei} value at which the
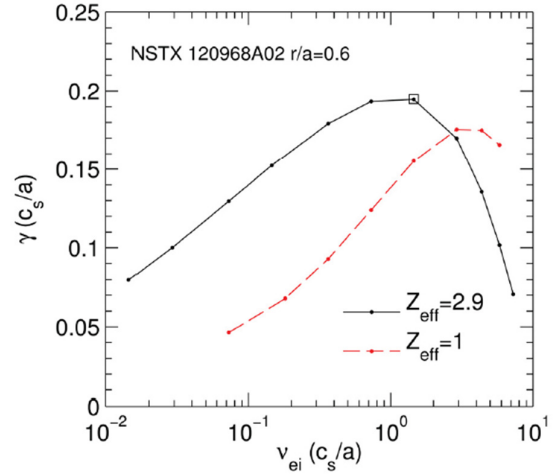
**Figure 5.** Linear growth rates verses ν_{ei} (defined using $Z_{eff} = 1$). Square symbol represents the experimental value. Reproduced from [35], with the permission of AIP Publishing.

$Z_{eff} = 2.9$ case has the peak linear growth rate. This shows that it is the total electron–ion collision frequency, namely $Z_{eff} \cdot \nu_{ei}$, that determines where the linear growth rate peaks with respect to ν_{ei}, since to obtain the same $Z_{eff} \cdot \nu_{ei}$ value, the $Z_{eff} = 1$ case would require a larger ν_{ei} than the $Z = 2.9$ case. The small reduction in the peak growth rate with $Z_{eff} = 1$ is likely due to enhanced potential perturbations from reduced adiabatic ion response, i.e. $\delta n_i/n_i \approx -Z_{eff}\delta\phi/T_i$. We would like to emphasize that the MT linear growth rate decreases with ν_{ei} below experimental value is qualitatively consistent with the global energy confinement scaling, $B\tau_E \sim \nu_e^{-1}$, observed in NSTX [15] and MAST [32]. Furthermore, qualitatively similar dependance of the MT mode linear growth rate on collisionality was also found at other radial locations [35].

Other linear parametric dependences of MT mode stability were also studied [35]. For example, figure 6 shows that the MT mode real frequencies and linear growth rates increase in these NSTX plasmas as the normalized electron temperature gradient, a/L_{T_e} ($L_{T_e} = (\mathrm{d}\ln T_e/\mathrm{d}r)^{-1}$ is the electron temperature gradient scale length) increases from 0.75 to 1.5 times of the local experimental value, demonstrating that the MT is driven unstable by the electron temperature gradient. Another finding worth mentioning is that the MT mode linear growth rate nonmonotonically depends on magnetic shear through the ratio $\hat{s}/q$. While decreasing at very large values ($\hat{s}/q > 2$), MT growth rates increase with $\hat{s}/q$ around the experimental values. This opposite trend to ETG scaling (to be discussed in the next section) for similar values provides an additional opportunity to distinguish these two modes experimentally.

One recent breakthrough in understanding anomalous electron thermal transport is the prediction of electron thermal transport dependance on collisionality using the first successful nonlinear gyrokinetic simulations of this high collisionality NSTX H-mode plasma using GYRO code as presented in [11, 36]. These careful numerical simulations have demonstrated numerical convergence in simulating the MT turbulence for the first time for NSTX and revealed that the key of achieving
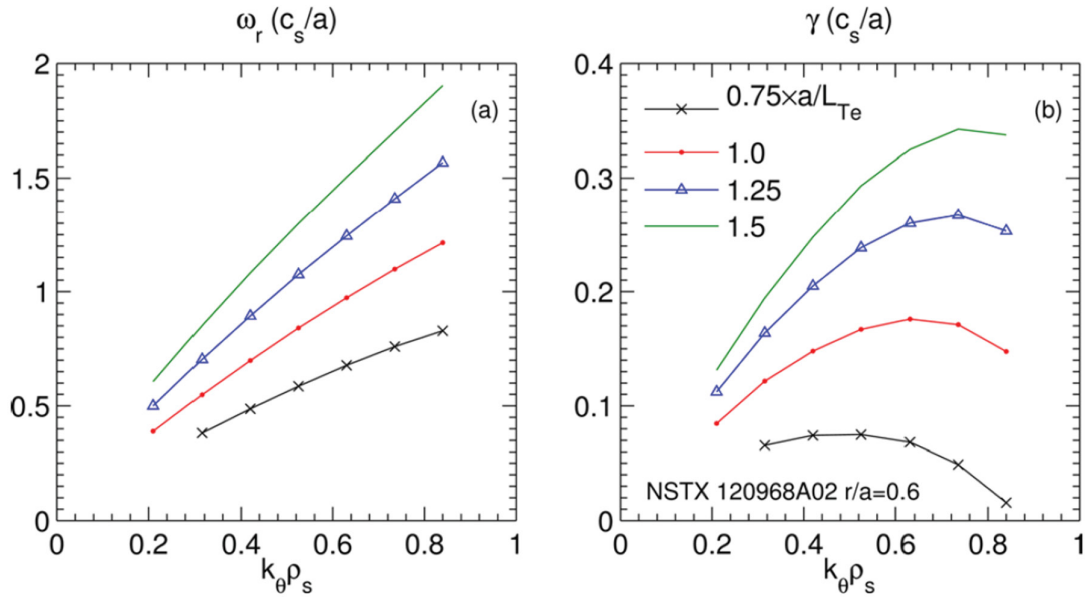
Figure 6. Linear microtearing growth rates versus $k_\theta \rho_s$ for varying normalized electron temperature gradient at $r/a = 0.6$. Reproduced from [35], with the permission of AIP Publishing.
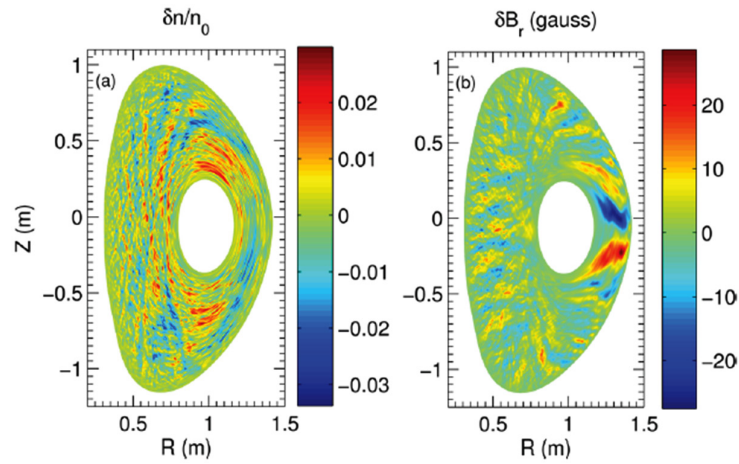

Figure 7. Snapshot of (*a*) normalized electron density perturbations and (*b*) δB_r (in Gauss) in a (R, Z) toroidal plane. Reproduced from [36], with the permission of AIP Publishing.

numerically sound results is to have enough radial resolution to resolve the narrow parallel current channel of the MT turbulence at each rational surfaces (some simplifications were used in these nonlinear simulations to minimize computational time, compared to linear simulations presented before; See [36] for details). Although the linear stability analysis shows that most unstable MT modes are at quite large toroidal mode numbers, e.g. $n = 30$ at $r/a = 0.6$, for these NSTX plasmas, nonlinear simulations show that there is a significant downshift in wavenumber spectral power to smaller mode number, i.e. an inverse cascade. This downshift manifest as poloidally broad fluctuation structure in electron density and B_r as shown in figure 7 which plots the toroidal cross section of the colored contours of the saturated electron density (see figure 7(*a*)) and B_r (see figure 7(*b*)) fluctuations. The dominant tordoidal mode number is seen to be about $n = 10$ for δB_r and is even lower for electron

density fluctuations, much smaller than that of the linearly most unstable mode. This nonlinear downshift in wavenumber spectral power is not surprising, and it has been observed in numerical simulations of other type of drift wave instabilities, e.g. ETG [40, 41]. Furthermore, the magnetic perturbations are spatially broad in both poloidal and radial directions, are much stronger on the outboard side (with instantaneous values ($\sim$25–30 Gauss) approaching 1% of the local equilibrium field ($\sim$3.5 kG)) and they become finer scale on the inboard side, which may allow easier detection through line-integrated Faraday rotation measurement (see [42]). In contrast, the density perturbations are narrow radially and the strength of the fluctuations is roughly uniform (statistically) around poloidal circumference, although they are elongated poloidally as the magnetic fluctuations.

The most important outcome from these nonlinear numerical simulations is that the MT turbulence is a candidate to
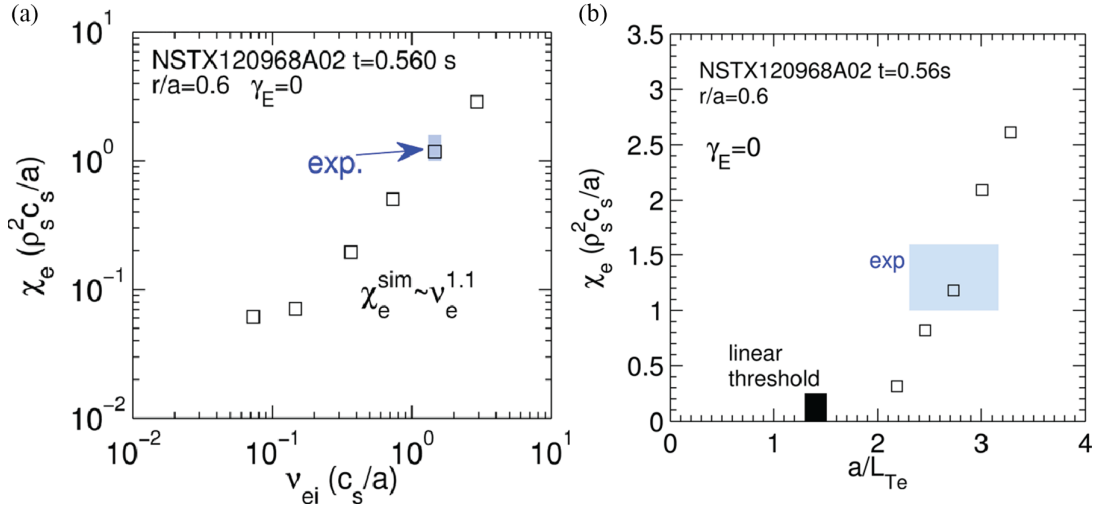
Figure 8. (*a*) Normalized electron thermal diffusivity versus normalized electron collision frequency (log–log scale). The shaded region shows the experimental values with uncertainties; (*b*) electron thermal diffusivity versus electron temperature gradient. The shaded region shows the experimental values with uncertainties. Reproduced from [36], with the permission of AIP Publishing.

explain observed electron thermal transport in these NBI-heated H-mode plasmas and the predicted electron thermal transport is in agreement with the observed confinement scaling. Figure 8 plots the predicted electron thermal diffusivity, χ_e, (normalized to the gyroBohm value) as a function of electron–ion collision frequency with variance from 0.005 to 2 times of the local experimental value with $Z_{eff} = 2.9$. It is clear from figure 8(*a*) that the predicted χ_e scales almost linearly with ν_{ei}, $\chi_e/(\rho_s^2 c_s/a) \sim (\nu_{ei} a/c_s)^{1.1} \sim \nu_e^{*1.1}$. This predicted scaling is in qualitative agreement with the scalings of linear growth rates, which vary by only ~3–4 over the same range of collisionality as shown in figure 5. This predicted nonlinear χ_e scaling is also in agreement with the observed confinement scaling dependence on collisionality [15, 30, 32], assuming a direct relation between local transport and global confinement, $\tau_E \sim a^2/\chi_e$. Furthermore, the amplitude of predicted χ_e is consistent with experimental value from power balance analysis. This agreement in magnitude and transport scaling provides evidence that the MT turbulence may play an important role in determining electron thermal transport in these NBI-heated NSTX H-mode plasmas. The stiffness in the electron thermal transport from the MT turbulence can be assessed from figure 8(*b*) where the predicted χ_e is plotted as a function of a/L_{T_e}. The fact that χ_e varies ±100% for ±20% change in a/L_{T_e} shows that the predicted transport is very stiff, which implies that profiles should adjust to be near marginal stability. This also suggests that it may be just as important to characterize the scaling of the MT threshold gradient. It is also found that $E \times B$ shear can significantly reduce predicted electron thermal transport by the MT even with a 20% increase in a/L_{T_e}, which complicates the interpretation of transport scaling from figure 8(*a*). However, including a carbon species in the simulations and non-local effects due to the large ρ^* in NSTX ($\rho^* \sim 0.01$) may influence the predicted results. Further nonlinear simulations incorporating new physics will be explored. In particular, an electromagnetic capability is being developed

for implementation in the particle-in-cell global gyrokinetic code, GTS [43] with an innovative electromagnetic numerical scheme [44], which will greatly facilitate our effort in investigating the role of the MT in driving electron thermal transport.

As we have said in section 1, the ultimate goal of studying the mechanism behind anomalous transport in fusion plasmas to achieve the predictive capability for the performance of future fusion devices so that optimization can be carried out. However, using full gyrokinetic simulations for such a problem is not practical in the foreseeable future given the present limitations in computer speed. In this regard, it is crucial to develop reduced models of different transport mechanisms since optimization requires iteration where efficiency in calculating transport coefficients is crucial. In earlier works [47, 48], electron thermal transport induced by the MT turbulence in NSTX was calculated using existing nonlinear theory [49, 50] and it was found to be in reasonable agreement with experiments. Recently, using the MT-mode-based Rebut-Lalia-Watkins (RLW) electron thermal diffusivity model, good agreement between experimental and predicted electron temperature profiles has been achieved in some NSTX high collisionality H-mode plasmas when the MT mode is found to be the dominant instability from linear microstability analysis [45, 46]. Figure 9 compares the maximum linear growth rate profile (top row) and predictability of T_e profile (bottom row) between a low collisionality and a high collisionality NBI-heated NSTX H-mode plasmas, respectively. Note that for the low collisionality plasma ($\nu_e^* \sim 0.06$, left panels), the most unstable drift wave modes are identified as a hybrid TEM/KBM (upper left panel). As a consequence, the predicted T_e profile by the RLW compares poorly with the experimental profile (lower left panel). On the other hand, for the high collisionality plasma ($\nu_e^* \sim 0.21$, right panels), the MT mode is found to be the dominant mode across most of the radial domain and the RLW prediction is in good agreement with the experimental profile from $x = 0.2$ to 0.8. It should be noted
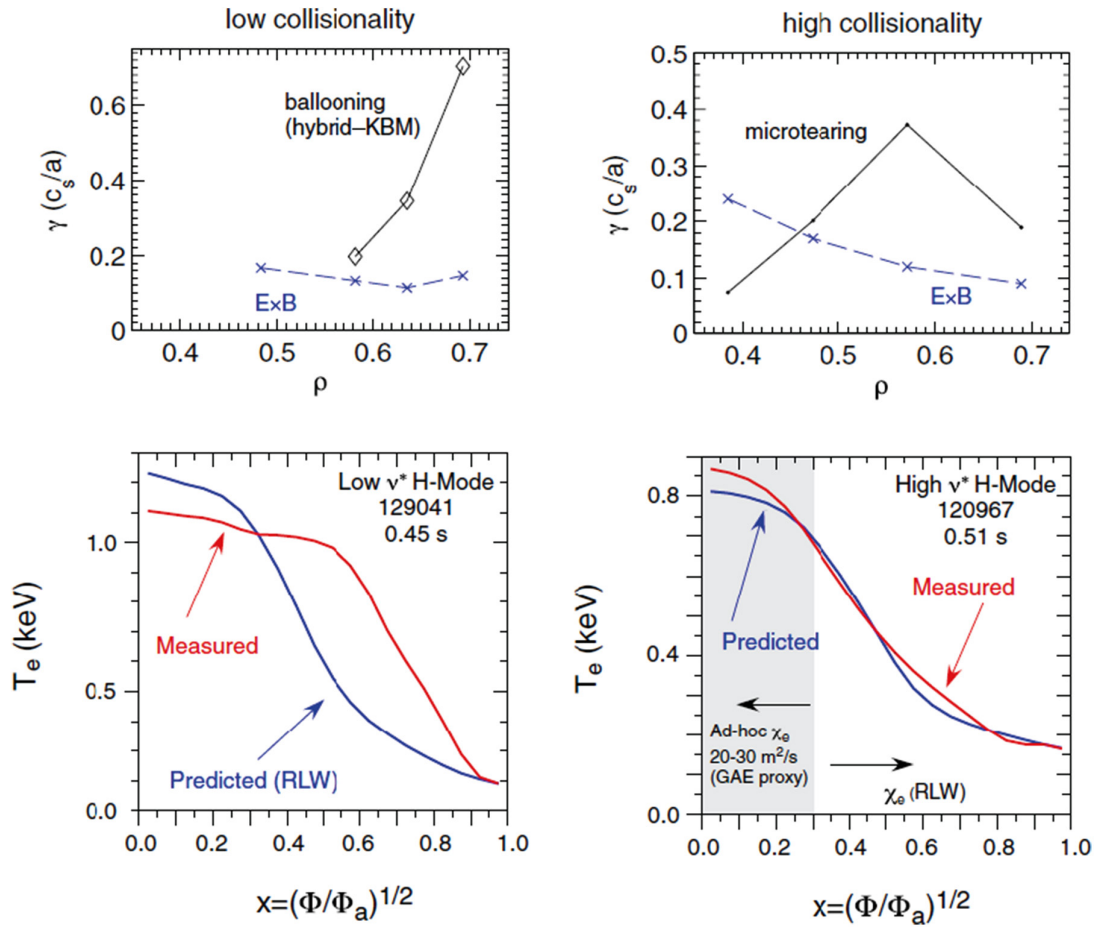
Figure 9. Linear growth rates (top) and measured versus predicted T_e using the RLW model (bottom) for a low (left) and high (right) collisionality H-mode discharge. In the top row, $\rho = r/a$, and the values correspond to x-values that are approximately 10% lower [45]. Figure from [46]. Reproduced from [45], with the permission of AIP Publishing.

that the radial coordinate $\rho = r/a$ used for the upper panels is the normalized poloidal flux and the $x = \sqrt{\Phi/\Phi_a}$ used for the lower panels is the square root of normalized toroidal flux. x is smaller than ρ by about 10%, namely $x = 0.6$ corresponding to $\rho \approx 0.7$. The RLW prediction was carried out for $x = 0.2$–0.8 with $x = 0.8$ as the boundary and an ad hoc χ_e was used inside $x = 0.2$ as a proxy for transport induced by AE activities in the very core [12, 13]. This successful prediction of T_e profile using the RLW reduced model provides the very first step towards predicting performance of future STs, e.g. FNSF.

2.2. Electron temperature gradient mode

The electron temperature gradient (ETG) mode has long been considered as a potential candidate in driving electron thermal transport [4, 5]. It was found that owning to its weaker secondary instability and zonal flow, ETG turbulence can drive much larger normalized thermal transport than ITG does [5, 20]. The ETG modes could be of particular importance to NSTX and NSTX-U since the large $E \times B$ shear tends to almost completely suppress low-k turbulence in NBI-heated H-mode plasmas. As we have discussed in section 1, ion thermal transport is consistently observed to be on the neoclassical level

for NSTX NBI-heated H-mode plasmas. On the other hand, ETG linear growth rates are usually much larger than $E \times B$ shearing rate and thus can survive the $E \times B$ shear stabilization (except for the case where the ETG mode is very close to marginal stability [51]; more discussion on this later in this section). As a result, the ETG mode is a natural candidate for driving electron thermal transport in NSTX/NSTX-U plasmas. Compared to the MT mode, the ETG mode is most likely the dominant mode in low-beta and low-collisionality plasmas and could be more important for NSTX-U due to the 3–6 times lower collisionality achievable on NSTX-U [25].
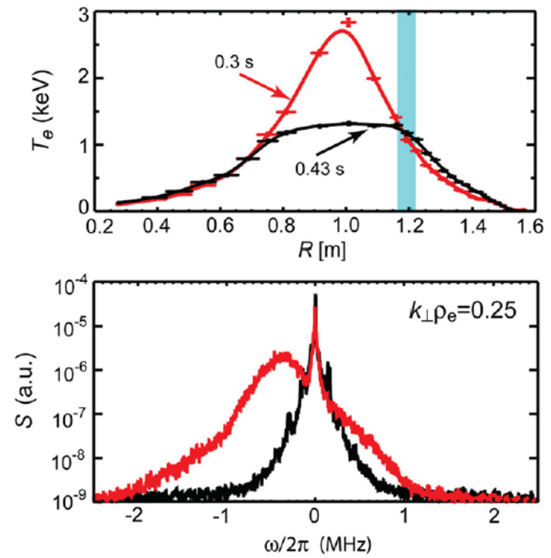
In NSTX, electron-scale turbulence was measured using a high-k microwave collective scattering system (the high-k scattering system) [52] (see figure 10). This was a large-angle scattering system which used 280 GHz microwave as the probe beam. The probe beam was injected tangentially into the plasma and plasma turbulence would scatter the microwave power according to Bragg condition. Due to this tangential scattering scheme, the scattering system measures mostly k_r components of plasma turbulence. By measuring scattering power and frequency shift (heterodyne receivers were used) at five individual channels that aims at different scattering angles (thus different wavenumbers), we were able to reconstruct wavenumber
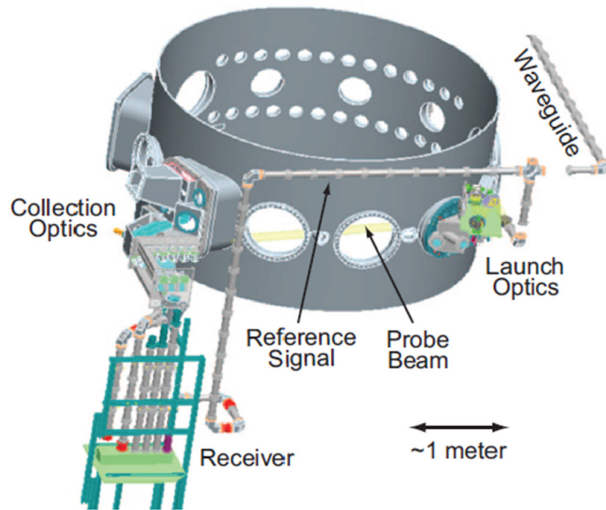
Figure 10. Arrangement of the NSTX collective scattering system. Reproduced from [52], with the permission of AIP Publishing.

Figure 11. Temperature profiles (top) and spectral density of fluctuations (bottom) at 0.3 s (red, with RF heating) and 0.43 s (black, without RF heating). The blue rectangle indicates the location of measurement region of the high-k scattering system where L_{T_e} is 15 cm and 50 cm, respectively. Negative frequencies (bottom) correspond to wave propagation in the electron diamagnetic direction. This is a NSTX RF-heated helium plasma with a minor radius of 0.65 m, a major radius of 0.85 m, an elongation of 2, a toroidal magnetic field of 0.55 T, a plasma current of 700 kA and an RF-heating power of 1.2 MW. Reproduced courtesy of IAEA. Figure from [54]. Copyright (2009) IAEA.

spectra of plasma turbulence (five data points along a line in the 2D plane of the k_r and k_θ wavenumber spectrum) and to determine the propagation direction of each wavenumber component, i.e. in the electron or ion drift direction. We note that although we did not measure the dominant spectral components of the ETG turbulence which are usually the modes with large k_θ and small k_r (see [40]), we assume that the spectral power at the wavenumbers measured by the high-k scattering system, i.e. large k_r and small k_θ, is positively correlated with that of the most dominant spectral component and this assumption is supported by nonlinear ETG simulations like the ones in [40, 53].

The first experimental evidence of the ETG mode on NSTX was observed in NSTX RF-heated helium L-mode plasmas using the high-k scattering system [54, 55]. Since the ETG mode is driven unstable by electron temperature gradient, the goal of these experiments was to use RF heating to vary a/L_{T_e}, so that the ETG mode stability could be changed. RF heating on NSTX mostly heats electrons and it can quite effectively change the local electron temperature gradient as shown in figure 11(*a*), where the T_e profiles with RF heating ($t = 0.3$ s) and without RF heating ($t = 0.43$ s) are plotted. It can be easily seen that the local electron temperature gradient is significantly larger $t = 0.3$ s (with RF heating) in the measurement region of the high-k scattering system (the high-k measurement region) denoted a blue rectangle. In particular, the L_{T_e} in the high-k measurement region increased from 15 cm at with RF heating to 50 cm without RF heating. Furthermore, T_e in the high-k measurement region remains essentially unchanged with and without RF heating, meaning that the same high-k detection channel measures the same normalized wavenumber ($k_\perp \rho_e = 0.25$) with and without RF heating ($k_\perp$ is the perpendicular wavenumber with respect to local magnetic field, namely $k_\perp = \sqrt{k_r^2 + k_\theta^2}$). This is reassuring that comparing scattering power changes from just one high-k detecting channel is meaningful. Figure 11(*b*) shows the frequency spectra of the scattering signal from a high-k detecting channel measuring $k_\perp \rho_e = 0.25$ with and without RF heating. We note that the

scattering power from plasma turbulence manifests itself as an off-center spectral peak for a typical frequency spectrum of a scattering signal, while the central spectral peak at $\omega/2\pi = 0$ is from spurious radiations, e.g. microwave power reflected by the NSTX vacuum vessel, that are not Doppler-shifted due to Bragg scattering from plasma turbulence. The fact that we almost always have some Doppler shift (from a combination of plasma toroidal rotation and turbulence propagation in the plasma frame) from scattering process greatly helped us distinguish real scattering power from the unwanted spurious radiation. It is clear from figure 11(*b*) that there is significant scattering power with RF heating and there is almost none without it, showing that the measured turbulence is positively correlated with the electron temperature gradient. In addition, the scattering signal has its peak at negative frequency which is the propagation direction of electron diamagnetic drift, consistent with that of ETG modes. Thus we consider these as strong pieces of experimental evidence of the presence of ETG modes in these RF-heated plasmas.

The natural next step is to assess if ETG mode stability indeed evolves as seen in the experiment. Linear stability analysis was carried out with the GS2 gyrokinetic code [56]. The GS2 code is an initial value gyrokinetic code which, in its linear mode, finds the fastest growing mode for a given pair of poloidal and radial wavenumbers. The normalized critical gradient $R/L_{T_e,\mathrm{crit}}$ (R is the major radius of the local flux surface) for the onset of the ETG modes was obtained by linear extrapolation of the growth rates of the most unstable modes
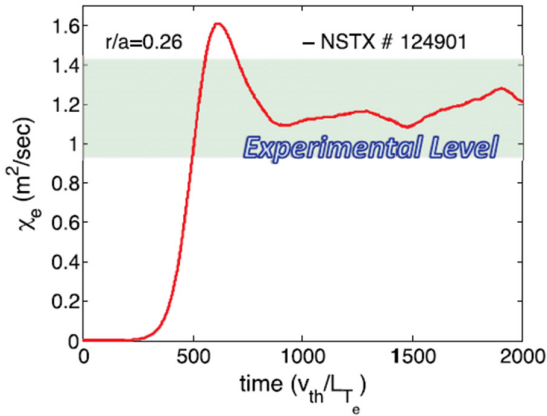
Figure 12. Time history of χ_e from a global ETG simulation of a RF-heated helium L-mode plasma similar to the case in figure 11 and comparison with experimental χ_e range (denoted by the shaded rectangular region) from power balance analysis. Reproduced from [41], with the permission of AIP Publishing.

calculated with several different temperature gradients [57]. It was shown that in the high-k measurement region, the experimental normalized T_e gradient, $R/L_{T_e,\mathrm{exp}}$, is larger than $R/L_{T_e,\mathrm{crit}}$ with RF heating at $t = 0.3$ s, while ETG modes become stable without RF heating at $t = 0.43$ s with $R/L_{T_e,\mathrm{exp}} < R/L_{T_e,\mathrm{crit}}$. The linear stability analysis of ETG modes is consistent with observed turbulence stability trend with respect to the change in R/L_{T_e}, strongly suggesting the existence of ETG turbulence in these RF-heated L-mode plasmas.

Beyond the linear stability analysis, the role of ETG turbulence playing in driving electron thermal transport was investigated using the particle-in-cell gyrokinetic tokamak simulation (GTS) code [43]. The GTS code is a global gyrokinetic code which calculates electrostatic turbulence in realistic tokamak configurations. Since global kinetic simulations of electron scale turbulence in a real tokamak geometry are very challenging, the global ETG simulation showed here used adiabatic ions and neglected coupling between ETG and low-k turbulence in order to keep computational cost to an acceptable level. Figure 12 plots the time evolution of GTS predicted χ_e which, after an initial overshoot, nonlinearly saturates to a level in agreement with the experimental range inferred from power balance analysis [41]. This agreement gives strong evidence that ETG turbulence plays an important role in driving electron thermal transport in these RF-heated L-mode plasmas. The simulation also revealed a direct energy channeling from ETG turbulence to e-GAM and low frequency zonal flows which may represent an effective mechanism for nonlinear ETG saturation. It is well known that ETG has weak direct dependence on electron collisionality. However, given this strong coupling with e-GAM and low frequency zonal flows, a dependence of ETG-driven electron thermal transport on electron collisionality could be introduced via collisional zonal flow and e-GAM damping, which is in analogy to the well-know paradigm of zonal flow regulating ITG turbulence and may lead to the scaling of confinement time proportional to $1/\nu_e^*$. This mechanism is subject to further investigation using

global nonlinear ETG GTS simulations with scans in electron collision frequency. We also note that such simulations have been performed in the context of MAST plasmas [58].

Having identified the likely existence of ETG turbulence in NSTX RF-heated L-mode plasmas, we have pursued further experimental parametric studies of ETG turbulence over the last couple of years of NSTX operation. The goal of these studies is to characterize ETG turbulence in different parametric regions, to validate reduced and first-principle models, and to find experimental tools to control ETG turbulence. In following, we present recent results of ETG turbulence dependence on $E \times B$ shear, electron density gradient, electron collisionality and magnetic shear [19, 51, 53, 54, 59, 60].

2.2.1. $E \times B$ shear dependence. $E \times B$ shear stabilization of ETG turbulence was not expected. Usually ETG modes have much higher linear growth rates than ion-scale modes, and thus the normal $E \times B$ shearing rate in tokamaks is not expected to have any effects on ETG modes. However, using the high-k scattering system, ETG turbulence stabilization from $E \times B$ shear was indeed observed [51]. It turns out that when ETG modes are close to marginal stability, the maximum linear growth rates can be quite low and comparable or even lower than the $E \times B$ shearing rate in NSTX H-mode plasmas, and thus ETG turbulence can be stabilized by $E \times B$ shear. Such an example is shown in figure 13 where the time evolution of electron-scale turbulence is compared with those of maximum linear growth rate (from GS2 calculations) and the Hahm–Burrell $E \times B$ shearing rate [61] (from TRANSP analysis [16]) for an NSTX NBI-heated H-mode plasma. Figure 13(*b*) clearly shows that scattering power from plasma turbulence (the off-center peak in the spectrogram) decreases significantly from about $t = 0.45$ s to 0.6 s. More details can be seen figure 13(*a*) which compares the frequency spectra at $t = 456$ and 592 ms (these two time points are denoted in the figure 13(*b*) with vertical solid lines with the same color). Furthermore, the frequency of the spectral peak falls on the right-hand side of the Doppler shift (due to plasma rotation), meaning that the turbulence mostly propagates in the electron direction consistent with that of ETG turbulence. The comparison between the normalized measured T_e gradient and GS2-calculated ETG critical T_e gradient in figure 13(*c*) shows that ETG turbulence is very close to marginal stability through the whole time period shown. Figure 13(*d*) plots the time evolution of $E \times B$ shearing rate and the maximum ETG growth rate, and it is clear that as the difference between the two becomes larger, the measured turbulence spectral power is reduced (see figures 13(*a*) and (*b*)). It is obvious from figures 13(*a*), (*b*) and (*d*) that the scattering power is much smaller at $t = 592$ ms when the ETG linear growth rate is significantly smaller than the $E \times B$ shearing rate. This result indicates that $E \times B$ shear may be an experimental tool to control ETG turbulence in future fusion machines, provided that ETG modes are close to linear stability threshold. We note that to fully assess the $E \times B$ shear effects on ETG turbulence in these NSTX plasmas, nonlinear gyrokinetic simulations are required, and they will be carried out in future studies.
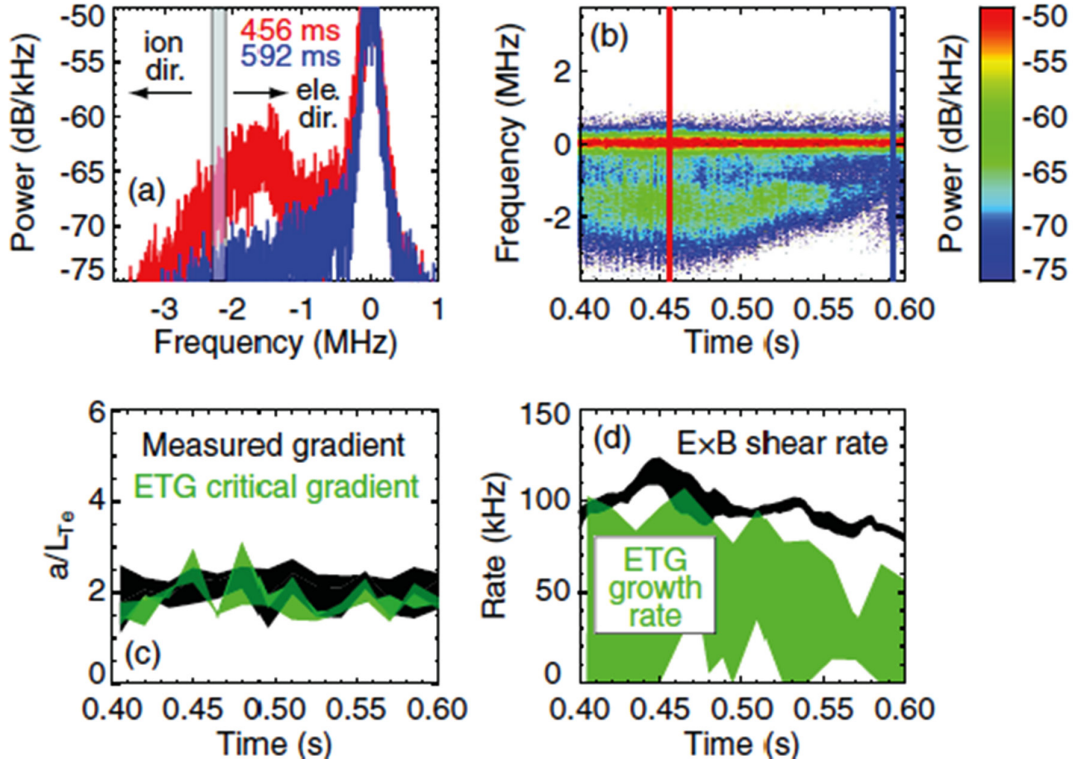
Figure 13. Fluctuation measurements and linear gyrokinetic calculations for a NSTX NBI-heated H-mode plasma in the high-*k* measurement region ($R = 133 \pm 2$ cm and $r/a = 0.5$–0.6); (*a*), (*b*) Fluctuation measurements with $k_\perp \rho_e \approx 0.27$–$0.3$. The gray rectangle marks the Doppler shift from toroidal rotation; (*c*) Measured electron temperature gradient and ETG critical gradient from GS2 calculations; (*d*) ETG linear growth rate and $E \times B$ shearing rate. The bands illustrate variations in the high-*k* measurement region. Reprinted figure with permission from [51], Copyright (2009) by the American Physical Society.

2.2.2. Density gradient dependence. Density gradient dependence of ETG modes has been predicted by theory (through parameter $\eta_e = \frac{\mathrm{d} \ln T_e}{\mathrm{d} \ln n_e}$ [4]) and gyrokinetic simulations [57]. In particular, an analytic form of the linear critical temperature gradient for ETG modes was derived with linear gyrokinetic simulations by varying individual parameters around sets of base case values from conventional tokamaks [57]:

$$(R_0/L_{T_e})_{\mathrm{crit}} = \max\left\{\left(1 + Z_{\mathrm{eff}}\frac{T_e}{T_i}\right)(1.33 + 1.91\hat{s}/q)(1 - 1.5\epsilon)\right.$$

$$\left.\times [1 + 0.3\epsilon(\mathrm{d}\kappa/\mathrm{d}\epsilon)], 0.8R_0/L_{n_e}\right\}$$

$$(1)$$

where R_0 is the major radius of the flux surface center, ϵ is the inverse aspect ratio and κ is flux surface elongation. Although we note that the geometric terms containing ϵ and κ in equation (1) may not be directly applicable to low aspect ratio tokamaks, the important point we want to emphasize is that the density gradient term ($0.8R_0/L_{n_e}$), if large enough, could determine the critical temperature gradient alone and result in the stabilization of ETG modes. Confinement improvements have been observed to be associated with peaked density profile resulting from pellet injection [62], and the improvements were attributed to density gradient, perpendicular flow shearing and/or reversed magnetic shear [63–65]. On NSTX,

we have presented the first direct experimental demonstration of density gradient stabilization of electron-scale turbulence [59]. The experimental observation is in quantitative agreement with linear numerical simulations and supports the conclusion that the observed density fluctuations are driven by ETG. Furthermore, it is found that the longer wavelength modes, $k_\perp \rho_s \lesssim 10$, are strongly stabilized by density gradient and that plasma effective thermal diffusivity is decreased by about a factor of two along with the stabilization. This finding of density gradient stabilization of the ETG turbulence suggests that the modification of density profile can be used to control ETG modes, a potential experimental knob.

The observation of density gradient stabilization of electron-scale turbulence was made around a large ELM event [66] (see the inserted D_α signal in figure 14(*a*)) in a deuterium H-mode plasma with 900 kA plasma current and 4.5 kG toroidal field. The particular interesting feature of this ELM event is that it led to a factor of 5 increase of normalized electron density gradient in the high-*k* measurement region while the changes in the other equilibrium quantities are much less. The steepening of density profile in the high-*k* measurement region (from about $R = 134$ to 139 cm) after the ELM event can be clear seen in figure 14(*a*) where the electron density profile is shown for $t = 498$ ms (before an ELM event) and $t = 532$ ms (after the ELM event) measured by multiple point Thomson scattering (MPTS) [67]. On the other hand,
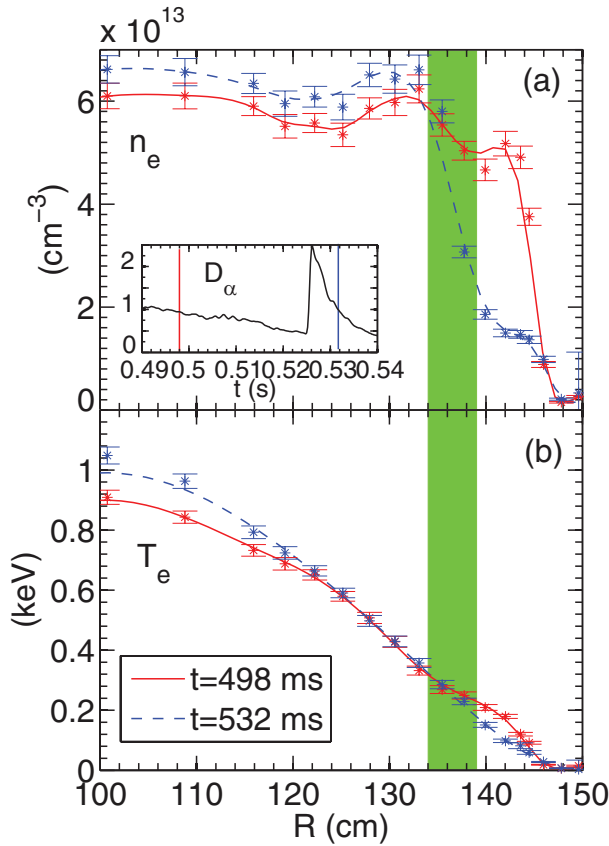
Figure 14. (*a*) Radial profiles of electron density at $t = 498$ and 532 ms which are before and after an ELM event (see the inserted D_α signal, where the two vertical lines denote the two Thompson time points); (*b*) Radial profiles of electron temperature at $t = 498$ and 532 ms. The shaded regions denote the measuring region of the high-*k* system. Large change in L_{n_e} after the ELM at $t = 532$ ms is evident. Reproduced from [59], with the permission of AIP Publishing.

only small change in electron temperature profile before and after the ELM event is seen in figure 14(*b*) and a/L_{T_e} actually increased in the high-*k* measurement region after the ELM event [59]). It was also found that magnetic measurements showed no large amplitude global MHD activity before, during and right after the ELM event.

A positive correlation between the electron-scale turbulence and electron thermal transport was observed before and after the ELM event as shown in figure 15. In figure 15(*a*) the measured electron-scale turbulence wavenumber spectra in arbitrary unit across the ELM event are shown for the three MPTS time points: $t = 498$, 515 (before the ELM event) and 532 (after the ELM event) ms, and reduced fluctuation spectral power after the ELM ($t = 532$ ms) at $k_\perp \rho_s \lesssim 15$ is evident with the most significant reduction, more than an order of magnitude, at small wavenumbers, $k_\perp \rho_s \lesssim 10$. We note that at $t = 532$ ms, estimated upper bounds are plotted for channels 3 and 4 which corresponds to $k_\perp \rho_s$ of 12.5–14.5 and 10–12, respectively, since after the ELM event channels 3 and 4 have scattering signals below the noise level. This stabilization of the electron-scale turbulence is found to be accompanied by a reduction in electron thermal diffusivity, χ_e, (calculated using

power balance analysis using the TRANSP code [16]) as shown in figure 15(*b*). It can seen in figure 15(*b*) that χ_e is reduced by a factor of about two after after the ELM at $t = 532$ ms in the high-*k* measurement region, correlated with reduction in the peak wavenumber spectral power after the ELM event seen in figure 15(*a*). The uncertainty in calculated χ_e is mainly due to uncertainties in ohmic heating and measured kinetic profiles. This observed positive correlation between the electron-scale turbulence and electron thermal transport indicates that the reduction in the relatively longer wavelength modes, $k_\perp \rho_s < 10$, may be responsible for the improvement in the electron thermal transport. On the other hand, we note that ion transport remains at the neoclassical level before and after the ELM event. We also note that although the more-than-an-order-of-magnitude reduction in the measured electron-scale turbulence spectral power at $k_\perp \rho_s \lesssim 10$ after the ELM event is much more than the factor of about two reduction in χ_e, additional mechanism beyond ETG turbulence is found to be necessary to account for the observed electron thermal transport after the ELM event as discussed below (see the discussion with regard to figure 17(*b*)).

Since the electron density gradient has the largest change in the high-*k* measurement region compared to other equilibrium quantities across the ELM event, the density gradient effects on the ETG mode linear stability was assessed with the GS2 code using local Miller equilibria [68] before and after the ELM events. In particular, the critical ETG calculated using the GS2 code, $(R_0/L_{T_e})_{crit,GS2}$, and measured normalized T_e gradient, $(R_0/L_{T_e})_{measured}$, in the high-*k* measurement region are plotted in figure 16 for the three MPTS time points. It is clear in figures 16(*a*) and (*b*) that before the ELM, i.e. $t = 498$ ms and 515 ms, $(R_0/L_{T_e})_{measured}$ is larger than $(R_0/L_{T_e})_{crit,GS2}$ for the most part of the high-*k* measurement region. However, at $t = 532$ ms (*c*), after the ELM, $(R_0/L_{T_e})_{crit,GS2}$ is much larger than $(R_0/L_{T_e})_{crit,GS2}$ in most of the high-*k* measurement region, showing that ETG modes are linearly stable in the most part of the high-*k* measurement region. This linear stabilization of ETG modes in the high-*k* measurement region is consistent with the observed large reduction of spectral power for $k_\perp \rho_s < 10$ at $t = 532$ ms as shown in figure 15(*a*). Further linear stability analysis was carried out to demonstrate the stabilization effect of the density gradient on the ETG modes by reducing R_0/L_{n_e} by 3, 4.5 and 6 units. As shown in in figure 16(*c*), lowering R_0/L_{n_e} by 3 units leads to significantly lowered critical T_e gradients in the high-*k* measurement region. It is also shown that the decreases to $(R_0/L_{n_e} - 4.5)$ and $(R_0/L_{n_e} - 6)$ lead to further reduction of critical R_0/L_{T_e} at $R > 135.5$ cm. However, only small change in critical R_0/L_{T_e} is observed at $R \lesssim 135$ cm with $(R_0/L_{n_e} - 4.5)$ and $(R_0/L_{n_e} - 6)$, which is consistent with the first term in the 'max' function on the RHS of equation (1) dominating the critical R_0/L_{T_e} as the second density gradient term becomes sufficiently smaller.

In order to compare the ETG-driven electron thermal transport with the experiment, local nonlinear gyrokinetic ETG simulations were carried out using the GYRO code with the same local Miller equilibria as used for the linear stability analysis above and the comparison with experimental electron
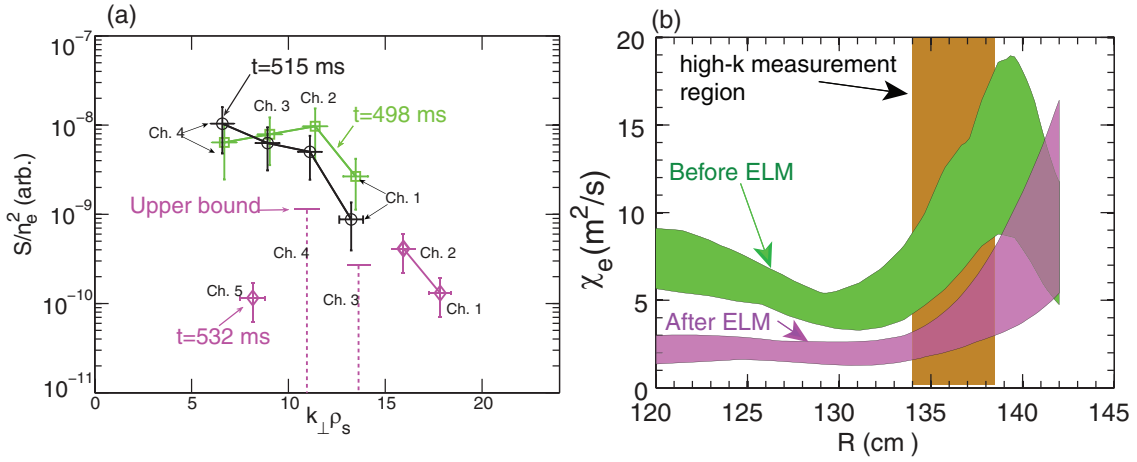
Figure 15. (*a*) The $k_\perp$ spectra at three MPTS time points: $t = 498$, 515 and 532 ms with the last time point after the ELM event (S is the spectral density). The absolute upper bounds for the density fluctuation spectral power are denoted by horizontal solid lines on the tops of vertical dashed lines.; (*b*) The electron thermal diffusivity as a function of R before the ELM at $t = 498$ (green) and after the ELM at $t = 532$ (magenta) with the shaded region denoting the high-k measurement regions. Reproduced from [53], with the permission of AIP Publishing.
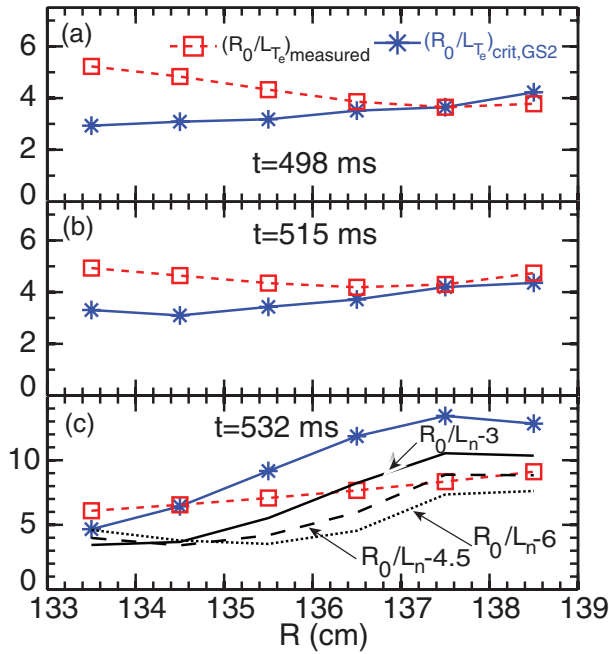

Figure 16. The critical T_e gradients calculated by GS2, $(R_0/L_{T_e})_{crit,GS2}$, (asterisks) in comparison with the measured temperature gradient, $(R_0/L_{T_e})_{measured}$, (open squares) in the high-k measurement region: (*a*) at $t = 498$ ms; (*b*) $t = 515$ ms; (*c*) $t = 532$ ms. Additional lines in (*c*) denote $(R_0/L_{T_e})_{crit,GS2}$ calculated with $(R_0/L_{n_e} - 3)$ (solid line), $(R_0/L_{n_e} - 4.5)$ (dashed line) and $(R_0/L_{n_e} - 6)$ (dotted line). Here, $(R_0/L_{n_e} - x)$ means that the normalized density gradient used in stability calculations is reduced by x units from the experimental value where $x = 3$, 4.5 or 6. Reproduced from [53], with the permission of AIP Publishing.

heat flux, Q_e, is shown in figure 17(*a*). The experimental electron heat flux from power balance analysis is represented by the solid blocks whose height denotes the experimental uncertainty and whose width denotes the range of density gradient for the radial region of $R = 133.5$ to 135.5 cm, the inner half

of the high-k measurement region which nonlinear simulations were carried out for. The solid blocks clearly show that after the ELM event, experimental Q_e decreased by about 1 MW and both the density gradient and its range increased significantly. We note that the reduction in Q_e after the ELM is mostly due to the decrease in electron and ion coupling, and larger radiation loss and dW_e/dt (W_e is the electron thermal energy) also contributed. The nonlinear simulations based on 'before ELM' and 'after ELM' parameters show a significant reduction in predicted Q_e after the ELM, which is qualitatively consistent with the experimental observation. Nonlinear simulations with scans in density gradient, i.e. the density gradient increased by 1.5 and 2 times based on the 'before ELM' parameters and reduced by 1/3 and 2/3 based on the 'after ELM' parameters, confirmed our expectation that the increase in density gradient is responsible for the reduced experimental Q_e after ELM as shown in figure 17(*a*). For example, a factor of 3 reduction in density gradient resulting in an order of magnitude increase in Q_e is seen in the scan based on the 'after ELM' parameters.

It is clear in figure 17(*a*) that the nonlinear ETG simulations based on nominal experimental parameters consistently under-predict Q_e comparing to the experimental values. Figure 17(*b*) shows simulation-predicted Q_e's with 20% and 40% increase in a/L_{T_e}. The simulations show that before the ELM, increasing a/L_{T_e} by 20% led to more than doubled predicted Q_e while by increasing a/L_{T_e} by 40% the predicted Q_e is already at the upper bound of the experimental value. On the other hand, after the ELM, with a/L_{T_e} increased by 40%, predicted Q_e still cannot match the experimental values. Thus, an additional mechanism may be needed to account for this discrepancy. We note that after the ELM event, ion-scale TEM was shown to be the most unstable mode [53], which is consistent with well-known density gradient destabilization of TEM [65], and the maximum linear growth rate of this TEM actually exceeds the $E \times B$ shearing rate. However, a recent global nonlinear ion-scale GTS simulation shows that this
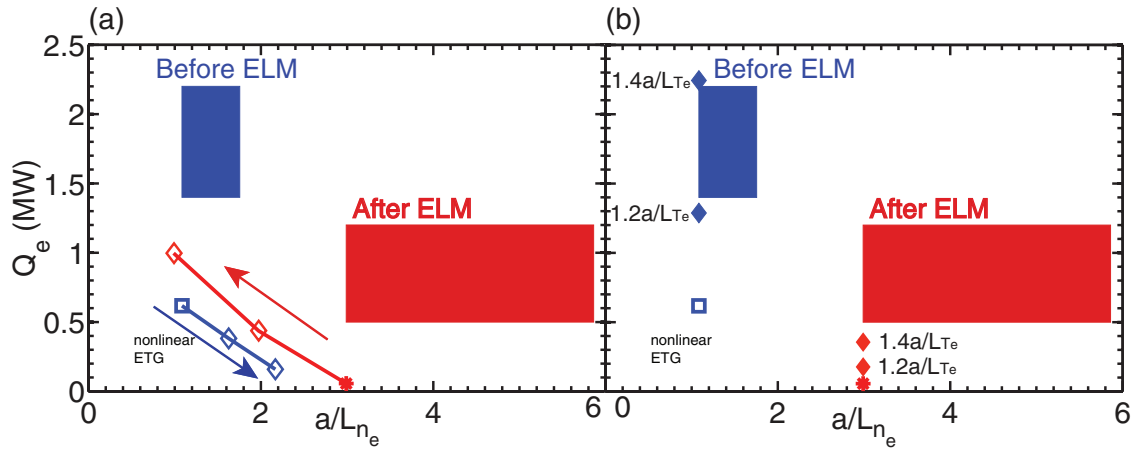
Figure 17. (*a*) Experimental electron heat flux from TRANSP analysis (solid rectangles) and calculated Q_e from nonlinear GYRO simulations (asterisk and open square) before the ELM ($t = 498$ ms) and after the ELM ($t = 532$ ms). Parametric scans (open diamonds) in density gradient based on 'before ELM' and 'after ELM' parameters are also shown. (*b*) The same as (*a*), except that parametric scans are in a/L_{T_e}. Reproduced from [53], with the permission of AIP Publishing.

TEM is not able to generate experimental level of electron thermal transport [41]. The reason behind this discrepancy is still being investigated.

More recently, the mechanism of density gradient stabilization of ETG turbulence is further confirmed in another set of NSTX H-mode plasmas [69], where the density gradient enhancement is induced by a plasma current ramp-down. The unique part of this finding is that ETG turbulence reduction is observed in correlation with the increase of density gradient while the measured electron temperature gradient remains larger than the critical temperature gradient calculated by the GS2 code. This indicates that density gradient can also nonlinearly stabilize ETG turbulence, in addition to the linear stabilization effects reported in [59]. This experimental observation of nonlinear stabilization by density gradient is shown to agree with local nonlinear ETG GYRO simulations using experimental equilibria [69] and is also consistent with nonlinear simulations on nonlinear stabilization of ETG turbulence by density gradient reported previously in [53].

2.2.3. Collisionality dependence. Due to the observed strong collisionality dependence of energy confinement time observed in STs [15, 32], it is also of great interest to study the collisionality dependence of ETG turbulence. Although the MT modes, as discussed in section 2.1, have a quite straightforward dependence on electron collisionality from its destabilization mechanism, it is still unknown whether the MT modes would be the dominant instability as collisionality gets into the lower collisionality regime of future spherical tokamaks [1, 25], and ETG modes may become a competing source of anomalous electron thermal transport. It is well known that the linear ETG instability should not be affected by electron collisionality as long as $\omega \gg \nu^{e/i}$. However, the situation is more complicated nonlinearly, and an analytical analysis in [70] shows that the collisional damping of ETG-mode-driven zonal flow could lead to stronger ETG turbulence/transport as collisionality increases, which is consistent with the experimental scaling. Particularly, the strong

coupling with zonal flow and e-GAM was observed in global ETG simulations of NSTX plasma [41] as discussed above. In addition, the dependence of ETG turbulence on collisionality has been observed in particle-in-cell gyro-kinetic simulations [71] and more recently in [58]. Here we review our results on this dependence from a collisionality scan carried out using low-beta NSTX NBI-heated H-mode plasmas with ρ_e, β_e and q_{95} kept approximately constant. The low-beta feature of these plasmas renders the MT modes stable, as confirmed by linear gyrokinetic analysis.

The collisionality scan was carried out following an established experimental procedure in NSTX [15] by varying B_T and I_p simultaneously with constant B_T/I_p and keeping density approximately constant. The low collisionality shots have $B_T = 4.5$ kG and $I_p = 900$ kA, and the high collisionality shots have $B_T = 3.5$ kG and $I_p = 700$ kA. In order to keep local ρ_e and β_e constant in this collisionality scan, we need to keep T_e/B^2 locally constant, where B is the total local magnetic field strength. Figure 18(*a*) plots the T_e profiles at $t = 367$ ms for the two low collisionality shots (141007 and 141040) and at $t = 332$ ms for the two high collisionality shots (141031 and 141032). The collisionality variation almost exclusively comes from changes in T_e, as higher T_e in the high-k measurement region for the low collisionality shots is seen than for the high collisionality shots (density difference is small). Figure 18(*b*) shows he normalized T_e/B^2 profiles, where good overlap among the profiles in the high-k measurement region is seen. We note that B profiles used to calculate T_e/B^2 are from LRDFIT equilibrium reconstructions constrained by MSE measurements [38, 72].

A factor of about 2.5 was achieved in the collisionality scan. In figure 19, the local ρ_e and β_e, q_{95}, and normalized energy confinement time, $B_T\tau_E$, are plotted as functions of local electron collisionality, ν_e^* (These local values are the mean values evaluated in the high-k measurement region). It is clear from figures 19(*a*)–(*c*) that ρ_e, β_e and q_{95} were kept relatively constant with less than 15% variation in the scan. As shown in figure 19(*d*), the normalized confinement time, $B_T\tau_E$,
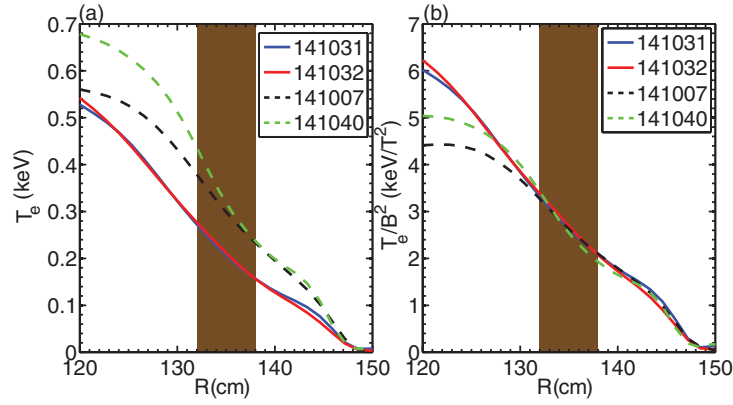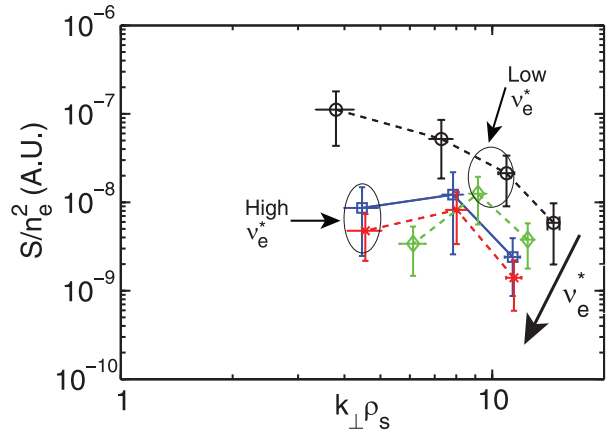
Figure 18. (*a*) T_e profiles measured by MPTS at times of interest for the 4 shots used in the analysis ($t = 367$ ms for the low collisionality shots 141007 and 141040; $t = 332$ ms for the high collisionality shots 141031 and 141032); (*b*) Normalized T_e/B^2 profiles for the 4 shots. The shaded regions in the figures denote the high-k measurement region. Reproduced from [53], with the permission of AIP Publishing.
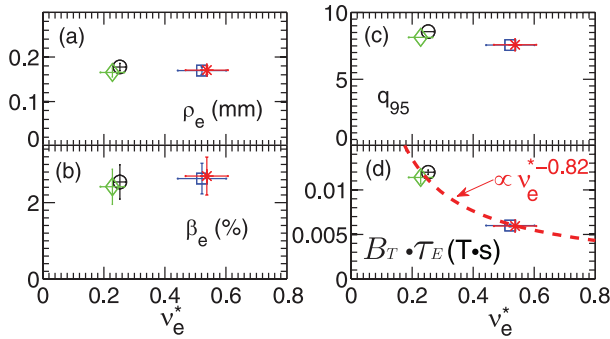
Figure 19. (*a*) Local electron gyroradius, ρ_e, (*b*) local electron beta, β_e, (*c*) q_{95}, (*d*) normalized energy confinement time, $B_T \tau_E$, all as a function of electron collisionality, ν_e^* for shots 141031 (blue square), 141032 (red asterisks), 141007 (black circle), 141040 (green diamond). The local values shown in (*a*) and (*b*) are the mean values in the high-k measurement region. The vertical and horizontal error bars denote the variation of corresponding quantities in the the high-k measurement region (applicable to ρ_e, β_e and ν_e^*). The red dashed line in (*d*) denotes a best power law fit to the normalized confinement time versus collisionality, which gives $\nu_e^{*-0.82}$. Reproduced from [53], with the permission of AIP Publishing.

Figure 20. The $k_\perp$ spectra in arbitrary unit (normalized to n_e^2 and S is the spectral density calculated using the total scattered power in the spectra of each channel) for shots 141031 (blue square), 141032 (red asterisks), 141007 (black circle), 141040 (green diamond). The first 2 shots are of high collisionality and the latter 2 shots are of low collisionality. The direction of increase of collisionality is denoted by a black arrow. Reproduced from [53], with the permission of AIP Publishing.

decreases as collisionality increases, and a power law fitting with the form of $\nu_e^{*\alpha}$ yields $\alpha = -0.82$, which is in agreement with the previous result of $\alpha = -0.92$ [15].

However, the measured ETG turbulence wavenumber spectra show quite complicated dependence on electron collisionality. Figure 20 shows that an anti-correlation between measured turbulence spectral power and collisionality exists for $k_\perp \rho_s > 9$. On the other hand, the collisionality dependence of the turbulence spectra at $k_\perp \rho_s < 9$ is quite different with one low collisionality shot (green diamond) having smaller spectral power than the high collisionality shots in this wavenumber range. The reason for this spectral difference between the two nominally similar low collisionality shots, 141007 and 141040, may be due to a combination of differences in linear growth rate spectral shape and $E \times B$ shear between the shots (see [53] for more details). If we take into account this $E \times B$ shear stabilization of lower wavenumber fluctuations, the

measured electron-scale turbulence spectral power appears to increase as collisionality is decreased. This observation is obviously inconsistent with the observed confinement dependence on electron collisionality where the normalized confinement time increases as electron collisionality decreases. However, the understanding of this discrepancy is still incomplete. We would like to point out that although the change in the electron–ion collision frequency is much larger than the changes in the other equilibrium quantities in the scan, smaller changes in other parameters could still contribute to the observed change in turbulence, e.g. q and a/L_{n_e}. Furthermore, large profile variations in equilibrium quantities actually may make the contribution from ion-scale turbulence possible (see figure 23 in [53]). When both ion-scale and electron-scale instabilities contribute to electron thermal transport, very likely for the cases we are considering there, multi-scale simulations would be needed to address the electron-scale fluctuations nonlinearly driven by
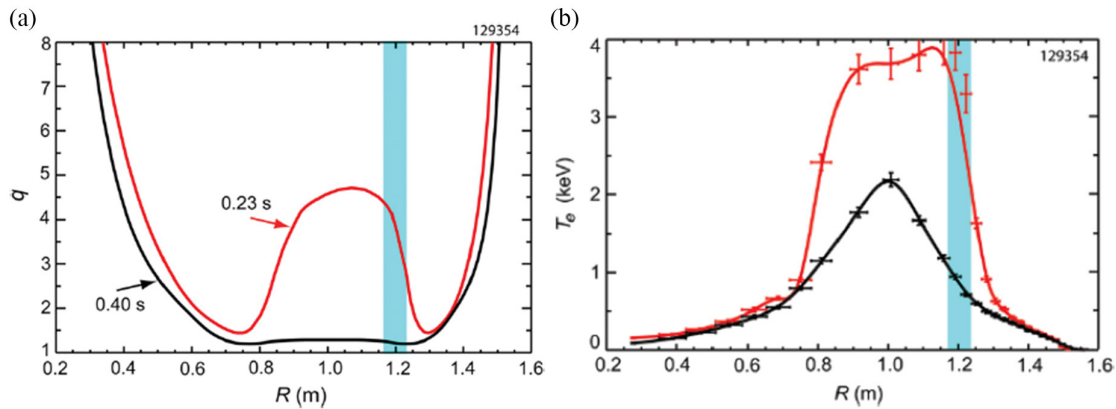
Figure 21. (*a*) q profiles on the equatorial plane with reversed magnetic shear (red) and after the collapse of reversed magnetic shear (black); (*b*) T_e profiles at the time of reversed shear (red) and after the collapse of reversed magnetic shear (black). The blue rectangle indicates the high-k measurement region. We note that 3 MW of RF heating is turned on at about $t = 150$ ms for this discharge. Reproduced courtesy of IAEA. Figure from [54]. Copyright (2009) IAEA.

ion-scale turbulence [73–75], which would be measured by the high-k scattering system. Global multi-scale simulations are very challenging, if not impossible, for the existing computational capabilities. Finally, we would like to point out that from what we have observed above, it is unlikely that ETG, ITG, TEM or MT modes alone would be able to explain the same dependence of confinement scaling on electron collisionality observed in different plasma regimes, and most likely, it is the interplay between these modes (i.e. multi-scale) and also global effect (i.e. profile variation) [76, 77] which are responsible for the observed confinement scaling.

2.2.4. Magnetic shear dependence. It is well-known that q profile affects tokamak plasma stability and confinement, e.g. forming internal transport barrier (ITB) due to reversed magnetic shear [78] and improving confinement in hybrid scenario characterized by a broad region of low magnetic shear [79]. Since electron thermal transport is particulary important for NSTX, studying how the ETG turbulence depends on q profile and magnetic shear, $\hat{s}$, is of great interest. In NSTX, the q profile can be varied by changing the current diffusion rate during the early phase of a plasma discharge when the plasma current is still diffusing from edge towards the center. A typical way to do this is to use high-power RF heating to significantly increase T_e (thus lowering resistivity) in the center so that diffusion of plasma current in the center is much reduced, forming a strong reversed magnetic shear region in the plasma center. This reversed magnetic shear phase usually lasts until an MHD instability starts to grow and results in a fast redistribution of the plasma current, thus flattening the q profile (see figure 21(*a*) for q profiles with and without reversed magnetic shear). During the phase of reversed magnetic shear, a steep gradient region is developed in the T_e profile near the location of minimum q (see figure 21(*b*)), showing the existence of an ITB in these plasmas. Figure 22 clearly shows that the electron-scale turbulence is suppressed in the ITB region with reversed magnetic shear (no obvious off-center frequency spectral peak is seen) and that the electron-scale turbulence appears (shown as frequency spectral peaks at $\omega/2\pi > 0$)

after the collapse of reversed magnetic shear. The propagation direction of the observed turbulence is in the electron diamagnetic drift direction after taken into account a >80 km s^{-1} plasma co-rotation, consistent with that of ETG turbulence. Furthermore, RF-heated-only ITB plasmas also show negligible $E \times B$ shear in the ITB region where electron-scale turbulence was found suppressed [60], demonstrating that reversed magnetic shear alone can suppress electron-scale turbulence. These observations strongly suggest that reversed magnetic shear can suppress electron-scale turbulence and the turbulence suppression is responsible for electron ITB formation.

The identification of the observed electron-scale turbulence as ETG-driven is supported by comparisons with results from gyrokinetic simulations. In [80], the amplitude of a electron-scale turbulence burst was resolved in time at three different frequencies by analyzing the scattering signal from the high-k scattering system with high time resolution (see figure 23(*a*)). The measured turbulence growth rates (derived from figure 23(*a*)) are shown in figure 23(*b*) and were found to occur at the electron sound speed scale (sound speed with electron mass) corresponding to a peak growth rate of 400 kHz. This peak growth rate, denoted by a star in figure 23(*c*), is consistent with the linear ETG mode growth rate from the GYRO calculation with the same values of R/L_{T_e} and magnetic shear, which strongly suggests that the observed electron-scale turbulence is ETG turbulence.

The suppression of ETG turbulence in electron ITBs is correlated with significant reduction in electron thermal diffusivity as shown in figure 24. Compared with a typical NSTX H-mode plasma, two electron ITB cases with $\hat{s} = -0.6$ and -1.6 show more than an order of magnitude reduction in χ_e. Furthermore, for the $\hat{s} = -1.6$ case, χ_e shows a weak dependence on R/L_{T_e} above ETG linear stability, while the $\hat{s} = -0.6$ case, χ_e increases modestly with R/L_{T_e}. It was noted that the increase in χ_e with R/L_{T_e} was accompanied by an increase in ETG bursts which is consistent with ETG-driven electron thermal transport.

Both local and global nonlinear gyrokinetic simulations of these reversed shear plasmas using the GYRO code were
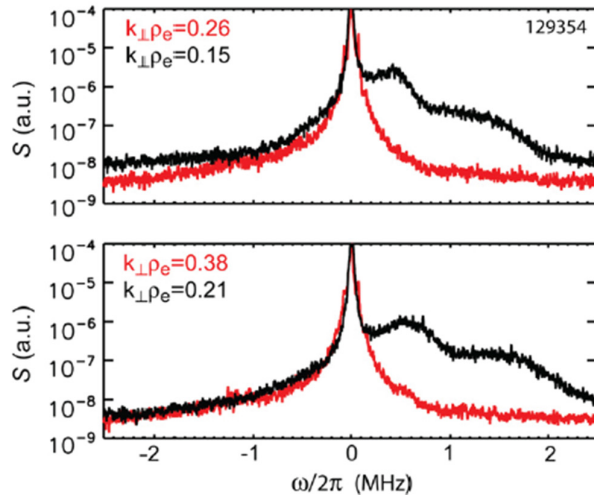
Figure 22. Electron-scale turbulence wavenumber spectra with reversed shear ($t = 0.23$ s, red) and after the collapse of reversed shear ($t = 0.4$ s, black). Reproduced courtesy of IAEA. Figure from [54]. Copyright (2009) IAEA.

reported in [21, 82]. It is shown that local simulations identify a strongly upshifted nonlinear critical gradient for thermal transport that depends on magnetic shear (see figure 25). It was also shown that for all magnetic shear used, the upshift in the nonlinear critical gradient (z_c^{NL}) from the linear one (z_c) is very strong, and the upshift becomes stronger as the $\hat{s}$ becomes more negative, e.g. from 9 at $\hat{s} = -0.2$ to 13 at $\hat{s} = -2.4$. Global simulations show electron ITB formation can occur when the magnetic shear becomes strongly negative. The global simulations also show that while the ETG-driven thermal flux at the outer edge of the barrier is large enough to be experimentally relevant, the turbulence cannot propagate past the barrier into the plasma interior.

3. Electron thermal transport in the core flat region

The origin of the electron thermal transport in the core flat region in NSTX NBI-heated H-mode plasmas is not yet fully understood. However, it is known that the relatively flat density and temperature profiles, make all drift wave instabilities very weak if not stable in this region [83]. Thus any working mechanism must obtain free energy from another source rather than the conventional density and/or temperature gradients. One particular free energy source that is unique for this region is the fast particle population from the NBI heating. It was well demonstrated that the $E \leqslant 100$ keV NSTX neutral deuterium beams of up to 7 MW can produce a large number of super-Alfvénic fast ions whose velocity space gradient can destabilize a broad spectrum of Alfvén eigenmode (AE) activities via Doppler shifted cyclotron resonances [84, 85]. The first observation of the correlation between electron thermal transport and AE activity was reported in [12]. As shown in upper panels of figure 26, the frequency spectra from Mirnov coil measurements clearly show increased AE activity as NBI power was increased from 2 to 6 MW. Particularly for the 6 MW H-mode case, the AE activity in the 0.5–1.1 MHz
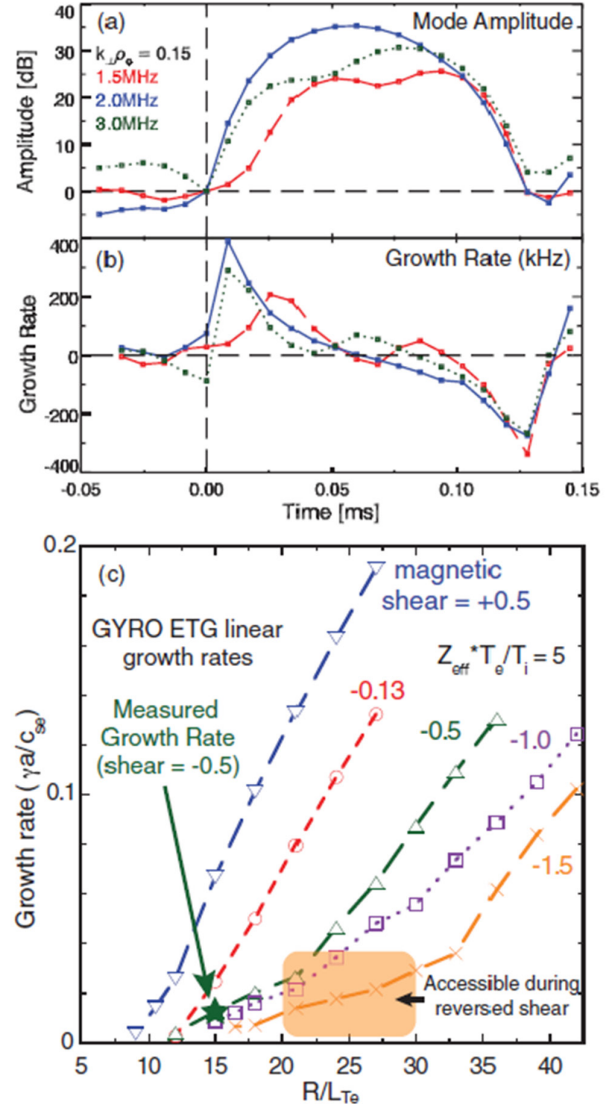
Figure 23. Time resolved mode amplitude of an ETG burst at three frequencies (*a*) and growth rate corresponding to mode amplitudes (*b*) from analyzing the scattering signal from the high-*k* scattering system with high time resolution; (*c*) GYRO computed growth rates, showing sensitivities to variations in magnetic shear and R/L_{T_e}. Star indicates measured growth rate at $\hat{s} = -0.5$. Reprinted figure with permission from [80], Copyright (2011) by the American Physical Society.
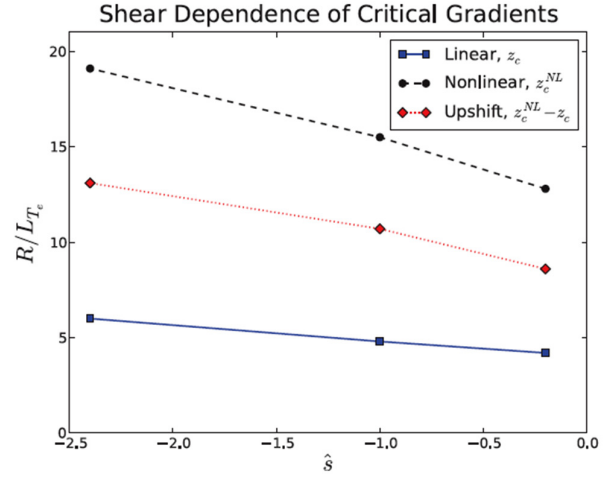
range was intense and broadband, while the lower frequency MHD activity was weak or absent including the toroidal Alfvén eigenmodes. The T_e profiles for different NBI heating power in figure 26 show that while the central T_e was kept almost constant as NBI heating power was varied, the T_e profile became broader as heating power was increased. This T_e flattening translates to significantly increased χ_e in the core region at higher NBI heating power from power balance analysis using the TRANSP code [16], as shown in the lower right panel in figure 26. Particularly, an order of magnitude increase in χ_e from an increase of NBI heating power from 2 to 6 MW is inferred. Given the lack of free energy source for conventional drift-wave-type micro-instabilities in this core flat
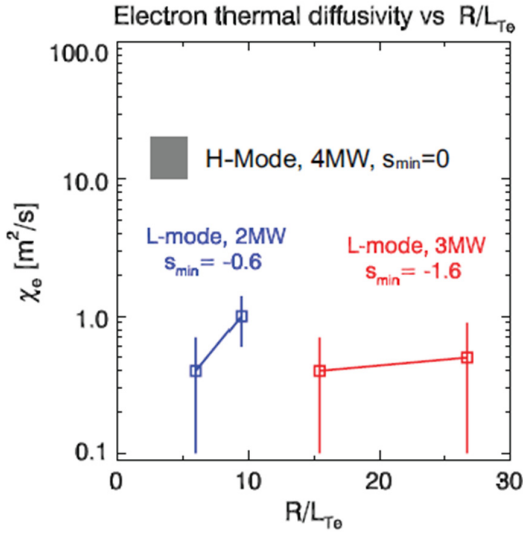
Figure 24. Electron thermal diffusivities from power balance analysis using the TRANSP code as functions of R/L_{T_e} for two electron ITBs and one typical NSTX H-mode plasma. These electron ITBs show low observed high-k activity at $\rho = r/a = 0.3$ ($R = 120\,\mathrm{cm}$). Reprinted figure with permission from [80], Copyright (2011) by the American Physical Society.

Figure 25. Critical gradients as a function of magnetic shear, $\tau = 1.8$ where $\tau = Z_{\mathrm{eff}}\frac{T_e}{T_i}$. ETG becomes linearly unstable at gradients above z_c (solid with square). Above z_c^{NL} (dashed with circles), turbulent thermal diffusivities exceed $1\,\mathrm{m^2\,s^{-1}}$. The dotted line with diamonds represents the nonlinear upshift of the critical gradient, $\Delta Z = z_c^{\mathrm{NL}} - z_c$. For comparison, the original cyclone ITG test case found an upshift in the critical gradient for transport that extended R/L_{T_i} by 2, from $z_c = 4$ to $z_c^{\mathrm{NL}} = 6$ at $\hat{s} = 0.78$ [81]. Reproduced from [82], with the permission of AIP Publishing.

region, the correlation between AE activity and T_e flattening implies that AEs may play an role in driving electron thermal transport. Furthermore, we note that in figure 26 some Mirnov coil frequency signal peaks intersect in time, which is a definite signature of global Alfvén eigenmode (GAE) [84, 85]. This is because GAEs have eigenfrequency in an approximate form of $\omega \simeq \pm v_{A0}(m/q - n)/R_0$ (v_{A0} is the Alfvén velocity, m and n are poloidal and toroidal mode numbers). When q is evolving in time, GAEs with different combinations of (m,n) will have different time dependences and thus the frequency peaks may intersect in time [84]. It is likely that both compressional Alfvén eigenmode (CAE) and GAE were present in that experiment but they were not distinguished in the experiment. Here we review the possibility of stochastic electron transport induced by GAEs [13] that as we argue are present among the unstable modes.

A model of how GAEs drive electron thermal transport was presented in [13] based on observations on NSTX presented above, where electron thermal transport is found to be induced by electron drift orbit stochasticity in the presence of multiple core localized GAEs. The basic logic behind this model is that since thermal ions do not interact with AEs due to their slow thermal velocity, any electron diffusion induced by the AEs would generate an ambipolar potential to prevent a net radial electron particle flux. With the ambipolar potential calculated using this constraint, an expression of the relation between the electron thermal diffusivity and particle diffusivity was identified (see details of the derivations in [13]). Thus electron thermal diffusivity can be inferred once the electron particle diffusivity due to the AEs is calculated, and this can be accomplished by using a guiding-center particle code ORBIT [86]. In these orbit simulations, the AE magnetic perturbations take

the form of $\delta B = R_0 \nabla \times (\alpha B_0)$ where B_0 is the equilibrium magnetic field, and the sum of the perturbations of AE modes is expressed as:

$$\alpha = \sum_{j=1}^{N} \alpha_j = \alpha_0 \sum_{j=1}^{N} \mathrm{e}^{-\mathrm{i}\omega_j t + \mathrm{i}m_j\theta - \mathrm{i}n_j\phi} \cdot \mathrm{e}^{-m_j^2(r-r_0)^2/(\delta r)^2} + \mathrm{c.c.}$$

(2)

where ω_j, m_j and n_j are the frequency, poloidal and toroidal mode numbers of the jth mode, and the radial structure is assumed to be Gaussian with a radial width of δr. α_0 is the amplitude for all the GAEs considered in the ORBIT simulations ($\alpha_0 = 4 \times 10^{-4}$ is the baseline case with characteristic values of $\delta B_r/B_0 \simeq 0.5 \times 10^{-2}$ and $\delta r = 0.4a$). Figure 27(a) plots the trapped electron motion Poincaré map in the plane ($\bar{\Psi}_\theta$, $\theta^0 = \omega_1 t + n\phi$) for one mode of ($m,n$) = (3, -1) at $f = 510\,\mathrm{kHz}$, where $\bar{\Psi}_\theta$ is the poloidal flux normalized to its edge value and $\theta^0 = \omega_1 t + n\phi$ is the phase of the AE mode. The Poincaré map of electron motion with the second mode added is shown in figure 27(b) with phase, $\theta^0 = \omega_1 t + n\phi$, determined by the first mode. Both cases show secular electron motion that is bounded in the radial direction. However, figure 27(c) clearly shows stochastic electron motion with 20 AE modes present in the simulation. Thus above simulations show that multiple AEs are needed to induce electron drift orbit stochasticity and thus electron thermal diffusion, which is supported by an initial experimental observation in NSTX [87].

The dependence of AE-driven electron thermal diffusivity on both the number of modes, N_{GAE}, and mode amplitude, characterized by α_0 were studied with ORBIT simulations. Figure 28(a) show the dependence of χ_e on the number of
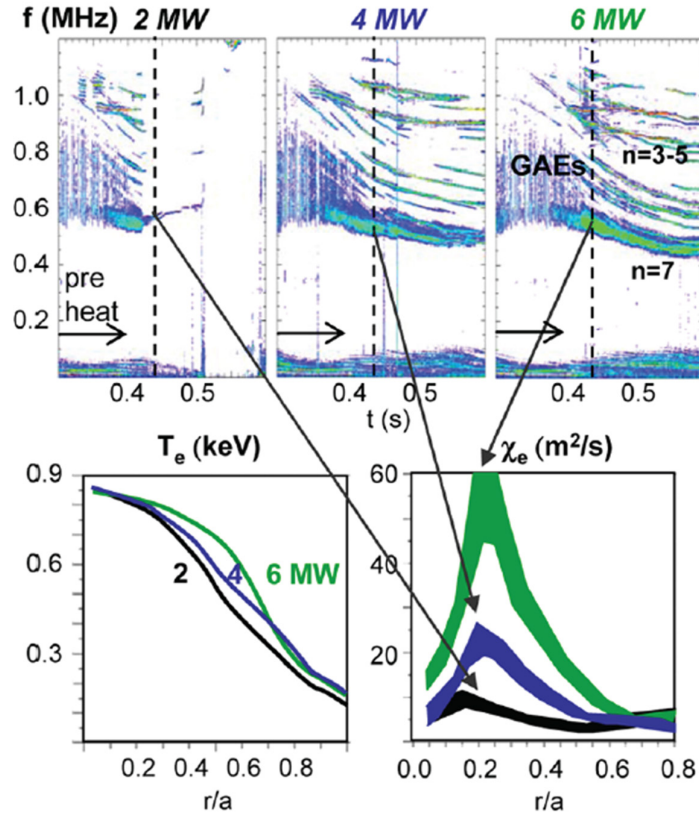
Figure 26. Correlation between GAE activity (upper panels), T_e (lower left panel) flattening, and central χ_e (lower right panel) increase in NSTX H modes heated by 2, 4, and 6 MW neutral beam, at $t \sim 0.44$ s. The vertical black dashed lines in the upper panels denote the time points at which the T_e and χ_e profiles are shown in the lower panels. Within the uncertainties, the q, n_e, and $E \times B$ profiles are the same in all discharges at the time of the transport correlation [83]. Reprinted figure with permission from [12], Copyright (2009) by the American Physical Society.
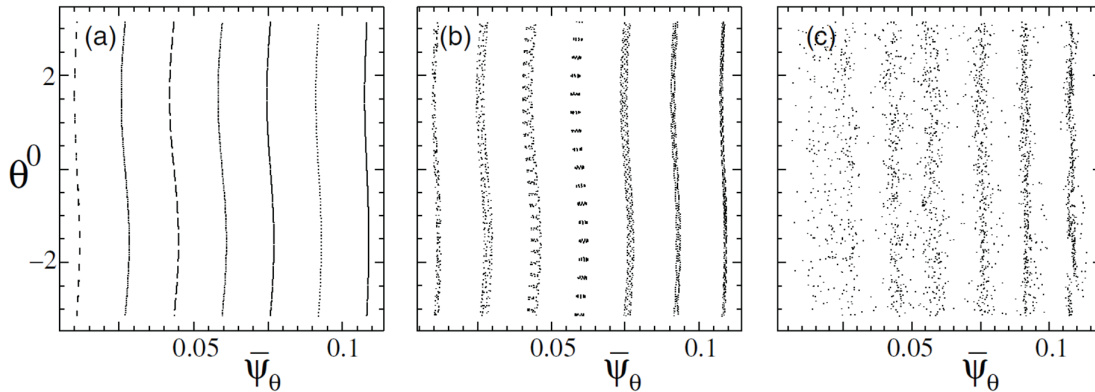
Figure 27. The electron Poincaré plot in the plane $(\bar{\Psi}_\theta, \theta^0 = \omega_l t + n\phi)$ with $\bar{\Psi}_\theta$ being the poloidal flux normalized to its edge value, with 1 AE mode (*a*), 2 AE modes (*b*) and 20 AE modes (*c*). The baseline case is considered with $\alpha_0 = 4 \times 10^{-4}$ and $\delta E_\parallel = 0$. Reproduced courtesy of IAEA. Figure from [13]. Copyright (2010) IAEA.

GAEs included in the simulations. The number of modes was increased by varying n from -1 down with m's varied to fit the 0.5–1 MHz frequency range observed in the experiment. It is clear from the figure that only a weak dependence of χ_e on N is seen at small N's, consistent with adiabatic electron motion. However, at $N > 16$, χ_e jumps by almost two orders of magnitude, and at $N \gtrsim 16$, χ_e seems to depend on N only weakly again. This result clearly shows that there is a

threshold in the number of modes for the stochasticity onset. Figure 28(*b*) shows a strong dependence of χ_e on α_0: $\chi_e \sim \alpha_0^3$ for $\alpha_0 < 5 \times 10^{-4}$ and $\chi_e \sim \alpha_0^6$ at higher mode amplitude, such as shown for $\bar{\Psi}_\theta = 0.05$. These strong mode amplitude dependences can induce intermittent strong electron thermal transport if the AE amplitude exhibits strong bursts for a short time period. The figure also shows that collisions have only minor effects at large mode amplitude, consistent with that

(a)   (b)
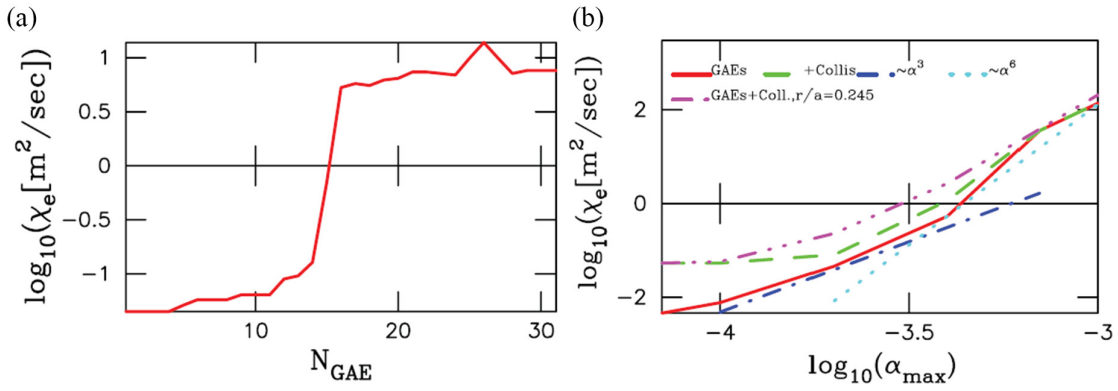
Figure 28. (*a*) Electron heat diffusivity dependence versus the number of applied GAEs. The results are obtained for the baseline case $\nu_e/\omega_{ce} = 6 \times 10^{-7}$, $\bar{\Psi}_\theta = 0.06$ and $\alpha_0 = 4 \times 10^{-4}$, where ω_{ce} is the electron angular gyrofrequency; (*b*) Electron heat conductivity versus GAE amplitude dependences. Solid curve corresponds to the χ_e without collisions at $\bar{\Psi}_\theta = 0.05$, dashed curve includes collisions, dash–dot–dot–dot curve includes collisions but is obtained at $\bar{\Psi}_\theta = 0.06$. For comparison, two lines, dash-dot and dot-dot, are plotted with α^3 and α^6 dependences. Reproduced courtesy of IAEA. Figure from [13]. Copyright (2010) IAEA.

collisional transport contribution is small in the tokamak core. It was shown in [13] that the radial dependence of the electron thermal diffusion is determined by the GAE structure assumed in simulations as it peaks near the mode localization region. In the simulations, $\chi_e > 10$ m^2 s^{-1} can be achieved with a mode amplitude $\alpha_0 > 4 \times 10^{-4}$, i.e. $\delta B_r/B_0 \gtrsim 0.5 \times 10^{-2}$. Although we do not yet have direct measurements of δB_r in the plasma core, newest experimental estimates based on reflectometer data [88] indicate a smaller mode amplitude, i.e. $\delta B_r/B_0$, than 0.5×10^{-2}. Thus qualitatively the AE activity may play an important role in driving electron thermal transport in the core flat region via the stochastic modification of thermal electron trajectories in the presence of unstable GAEs. We note that a more quantitative comparison between the model and experiments requires using measured or simulated mode structure and amplitude, which needs to be addressed.

We also would like to point out that more recently, another mechanism of explaining flattening T_e profile in high-power NSTX NBI-heated H-mode plasmas has been proposed [23]. This mechanism involves the coupling of core-localized CAE to kinetic Alfvén waves (KAWs) at the Alfvén resonance location at the edge of the fast particle density profile. These KAWs have large parallel electric fields at the Alfvén resonance location (see the $\delta E_\parallel$ radial profile in figure 29(*a*)), much larger than those of CAEs. The KAW parallel electric field can efficiently accelerate and heat electrons. This coupling between CAE and KAWs channels fast particle energy from its injection location in the core to the edge of the fast particle density profile and effectively change the electron heating profile from what would be expected from just the classical fast particle slowing-down (see the radial component of the Poynting flux vector profile in figure 29(*b*)). Particularly, seen in figure 29(*b*), the calculated change in energy flux due to the coupling to KAWs across the resonant surface at $R = 0.6$–0.7 m is about 1.5×10^5 W m^{-2} and, with estimated surface area of about 2–3 m^2, the calculated power absorption is about 0.3–0.5 MW, a significant fraction of the neutral beam power in NSTX (up to 2 MW per ion source). Furthermore, this mechanism also works more efficiently with multiple CAEs

since each CAE can couple to KAWs and provide the energy channeling. We also note that in addition to inducing effective energy channeling, the presence of multiple KAWs may also strongly enhance electron thermal transport due to finite $\delta E_\parallel$. Finally we note that since this coupling of core-localized CAE to KAWs is an ubiquitous process, the resulting energy channeling of this coupling can also happen in conventional tokamaks if CAEs are excited.

4. Summary and discussion

In summary, we have made significant progress in understanding electron thermal transport in the last couple years of NSTX operation, which includes the first successful nonlinear MT simulations of NSTX high-collisionality H-mode plasmas that predict electron thermal transport consistent with observed dependence of energy confinement scaling on electron collisionality [11, 35, 36], the first identification of ETG turbulence in NSTX RF-heated plasmas [55], extensive parametric studies of ETG turbulence in NSTX coupled with linear and nonlinear gyrokinetic simulations [53, 54, 59, 60, 69, 80], and the experimental observation and theoretical/numerical modeling of the correlation between the AE activity and the T_e flattening in NSTX high-power NBI-heated H-mode plasmas [12, 13, 23, 83]. We note that all progress was made possible by the synergy between experimental observations and theoretical/numerical modeling, which will also be the essential practice in the transport and turbulence research on NSTX-U [25]. The results reviewed here support our argument that an universal mechanism for explaining electron thermal transport in NSTX/NSTX-U does not exist due to the wide range of parameters that NSTX/NSTX-U can achieve with different operational scenarios. Thus the logical next step is to identify experimentally the operational regimes of different instabilities guided by linear and nonlinear gyrokinetic simulations. Our ultimate goal, of course, is to develop reduced models for the responsible instabilities so that prediction and optimization of energy confinement performance of future STs can be carried out. Although initial progress has been made for the
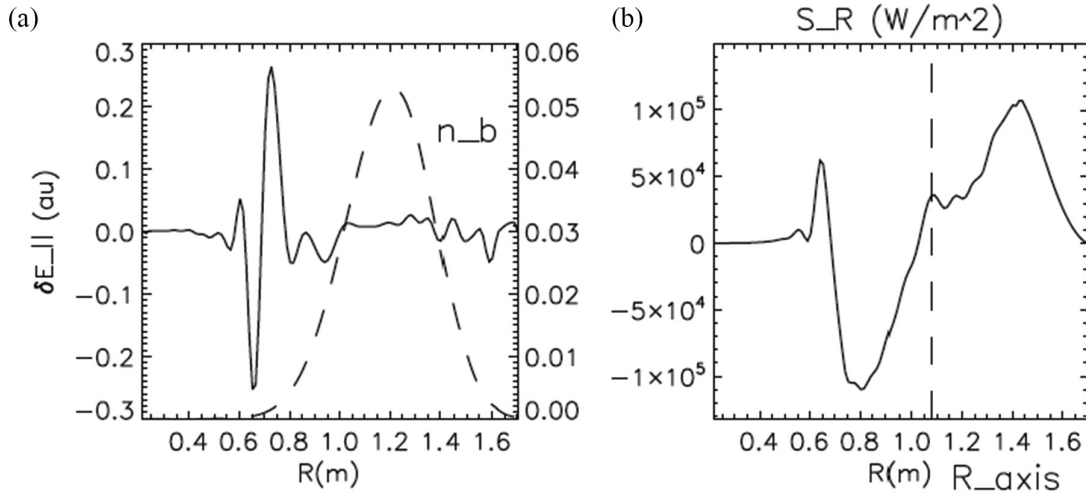
Figure 29. Radial profiles of $\delta E_\parallel$ (*a*) and radial component of Poynting vector $\vec{S} = \langle \vec{E} \times \vec{B} \rangle$ (*b*) for the $n = 4$ CAE mode from self-consistent nonlinear simulations near saturation. Reprinted figure with permission from [23], Copyright (2015) by the American Physical Society.

MT turbulence [45], reduced modes for ETG turbulence and the AEs in STs are still lacking.

The observed ST energy confinement scaling dependence of electron collisionality is obviously the most intriguing mystery in ST transport research. The inverse dependence of normalized energy confinement time on collisionality essentially means a better confinement at higher electron temperature. Given the fusion goal of achieving higher temperature, such a positive feedback is great for future STs if this confinement scaling can extend to even lower collisionalities, one of the main missions of the NSTX-U. The results reviewed here show that we have made significant progress towards understanding this collisionality dependence, such as the nonlinear simulation of the MT turbulence and the study of collisionality dependence of ETG turbulence. However, the issue is far from solved. We would like to point out that although the nonlinear MT simulations of NSTX high-collisionality H-mode plasmas have reproduced similar confinement scaling with experimental-level electron thermal transport [11, 36], the $E \times B$ shear stabilization effects on the MT modes have not been fully resolved and profile variation effects were not addressed in those local simulations. Furthermore, the MT turbulence has been shown to be weak in driving electron thermal transport in the collisionality regime of future STs, and thus other operational transport mechanisms have to be identified. More recently, the dissipative TEM (DTEM) has been shown to produce similar collisionality dependence for electron thermal transport in GTS simulations [22, 41] (although it was based on an NSTX H-mode equilibrium after a large ELM event [59]; analysis using more typical NSTX H-mode equilibria is being carried out [89]). One unique property of DTEM found in [22, 41] is that it is insensitive to $E \times B$ shear, in contrast to the initial finding on the $E \times B$ shear effects on the MT mode in [11]. However, the predicted electron thermal transport is still much less than what is observed in experiment [22, 41], although it is unknown if the electromagnetic effects that are not included in the GTS simulations could change the results. As a matter of fact, NSTX ion-scale gyrokinetic simulations

seem almost always under-predict electron thermal transport for NSTX plasmas with auxiliary heating (good agreement has been found for a case with only Ohmic heating, as presented in [90]). This implies that ion-scale turbulence alone may not be able to explain electron thermal transport and the observed collisionality dependence of the energy confinement scaling. As we discussed in section 2.2, ETG turbulence may have a collisionality dependence due to the coupling to low frequency zonal flow and e-GAM [41, 58, 71]. However, such a dependence has not been observed in the NSTX experimental collisionality scan and corresponding ETG simulations [53], where the observed change in electron-scale turbulence was attributed to the changes in parameters other than electron collisionality (although electron collisionality is shown to have the largest change among all equilibrium quantities). On the other hand, it is also possible that the factor of 2.5 change in electron collisionality may just be not large enough to induce significant change in ETG turbulence. The ETG dependence on collisionality will be studied further on NSTX-U. Cross-scale interaction between ion-scale and electron-scale turbulence could also be important as shown in [73, 75]. This interaction may not be as important for NSTX/NSTX-U as for conventional tokamaks, since ion-scale turbulence in NSTX was shown to be significantly suppressed due to large $E \times B$ shear. However, there are situations where ion-scale turbulence is non-negligible [22, 41, 53] and the multi-scale effects could be important. We note that a multi-scale simulation of NSTX/NSTX-U plasma will be a daunting task, much more expensive than those conducted for conventional tokamaks [75], but we, nevertheless, have plans to carry it out once a suitable target plasma is identified from future NSTX-U operations.

In addition to electron collisionality, other equilibrium parameter dependences were also identified to affect electron thermal transport and turbulence, including $E \times B$ shear, density gradient and magnetic shear. In particular, electron density gradient and magnetic shear were found to have stabilization effects on electron-scale turbulence and thus to improve plasma

confinement [54, 59, 60, 80], and these stabilization effects were shown to be consistent with the parametric dependence of ETG turbulence from linear and nonlinear gyrokinetic simulations. These results have important implications for NSTX-U and future STs. The second NBI on NSTX-U would allow us to have more control on the density and q profile by using different ion sources aiming at different tangential radius. Thus different density gradients and magnetic shear could be achieved in a more controlled fashion (compared to NSTX) to change ETG turbulence and possibly the electron thermal transport. These experimental knobs not only can be used to change a particular turbulence but also can be used to distinguish different turbulence through their parametric dependence. For example, the MT nd ETG modes have almost opposite dependence on $\hat{s}/q$ [26], and with a controlled scan of $\hat{s}/q$ in experiments, the two modes can be distinguished and so do their contributions to electron thermal transport.

We have also presented potential mechanisms that are responsible for the flattening of core T_e profile observed in NSTX high-power NBI-heated H-mode plasma, where conventional drift wave instabilities are found to be weak due to the flat profiles. One mechanism is an electron thermal transport model based on GAE/CAE induced electron drift orbit stochasticity and the other mechanism relies on the coupling between CAEs and KAWs to change electron heating profile. Both mechanisms can qualitatively explain the flattening of the core T_e profile, and both mechanisms work best with multiple AEs, which is consistent with initial experimental observations [87]. Experimental scans with beam power, toroidal magnetic field and plasma current on NSTX-U coupled with simulation predictions hopefully will clarify this issue. We also note that an analytic GAE mode structure was used in [13] and the mode amplitude was estimated. To compare better with experiments, the plan is to use measured mode structure and amplitude in ORBIT calculations. Furthermore, ORBIT calculations will also be coupled with GAE and CAE calculations using the HYM code [91]. These comparisons will not only allow us to distinguish the two different mechanisms but also will lead to the development of reduced models on the core T_e flattening.

Finally we would like to point out that NSTX-U will have much enhanced diagnostic capabilities that allow us to make new turbulence measurements. A 48-channel beam emission spectroscopy (BES) diagnostic [92] is already operational on NSTX-U, and a Doppler back scattering (DBS)/cross polarization scattering (CPS) diagnostic as well as a 693 GHz far infrared (FIR) high-k_θ scattering system are currently being developed. The DBS system [93] will provide intermediate-scale density fluctuation measurements bridging a wave-number spectral gap between the BES diagnostic and the high-k_θ scattering system, and the CPS system will measure internal magnetic fluctuations through the cross polarization scattering process [94–97]. The FIR high-k_θ scattering system is designed to achieve two scattering schemes which are sensitive to different regions of the turbulence 2D k spectrum thanks to the large magnetic shear in NSTX-U, which will allow the determination of the anisotropy in the 2D k spectrum of ETG turbulence, i.e. the existence of ETG streamers, by comparing the k spectra measured by two schemes. In addition,

a Multi-energy soft x-ray (ME-SXR) diagnostic [98] capable of providing fast ($>10\,$kHz) measurements of changes in the electron temperature and density profiles is also operational on NSTX-U, and it will be used to measure the fast T_e response to intermittent or bursting AE activities to further confirm the correlation between electron thermal transport and the AE activities. Coupled with a planned laser blow-off system, the ME-SXR diagnostic will allow the study of perturbative electron thermal transport in NSTX-U by measuring cold pulses propagation from non-recycling impurity injection. These diagnostic enhancement will greatly help us to achieve the goal of understanding electron thermal transport in STs.

Acknowledgments

References

[1] Menard J.E. *et al* 2011 *Nucl. Fusion* **51** 103014
[2] Horton W. 1999 *Rev. Mod. Phys.* **71** 735
[3] Connor J.W. and Wilson H.R. 1994 *Plasma Phys. Control. Fusion* **36** 719
[4] Lee Y.C., Dong J.Q., Guzdar P.N. and Liu C.S. 1987 *Phys. Fluids* **30** 1331
[5] Dorland W., Jenko F., Kotschenreuther M. and Rogers B.N. 2000 *Phys. Rev. Lett.* **85** 5579
[6] Coppi B. and Pegoraro F. 1977 *Nucl. Fusion* **17** 969
[7] Kadomtsev B. and Pogutse O. 1971 *Nucl. Fusion* **11** 67
[8] Tang W., Connor J. and Hastie R. 1980 *Nucl. Fusion* **20** 1439
[9] Hazeltine R.D. and Strauss H.R. 1976 *Phys. Rev. Lett.* **37** 102
[10] Drake J.F., Gladd N.T., Liu C.S. and Chang C.L. 1980 *Phys. Rev. Lett.* **44** 994
[11] Guttenfelder W., Candy J., Kaye S.M., Nevins W.M., Wang E., Bell R.E., Hammett G.W., LeBlanc B.P., Mikkelsen D.R. and Yuh H. 2011 *Phys. Rev. Lett.* **106** 155004
[12] Stutman D., Delgado-Aparicio L., Gorelenkov N., Finkenthal M., Fredrickson E., Kaye S., Mazzucato E. and Tritz K. 2009 *Phys. Rev. Lett.* **102** 115002
[13] Gorelenkov N., Stutman D., Tritz K., Boozer A., Delgado-Aparicio L., Fredrickson E., Kaye S. and White R. 2010 *Nucl. Fusion* **50** 084012
[14] Rewoldt G., Tang W.M., Kaye S. and Menard J. 1996 *Phys. Plasmas* **3** 1667
[15] Kaye S.M. *et al* 2007 *Nucl. Fusion* **47** 499
[16] Hawryluk R.J. 1981 *Physics of Plasma Close to Thermonuclear Conditions* (New York: Pergamon)
[17] Houlberg W.A., Shaing K.C., Hirshman S.P. and Zarnstorff M.C. 1997 *Phys. Plasmas* **4** 3230
[18] Stutman D. *et al* 2006 *Phys. Plasmas* **13** 092511
[19] Ren Y. *et al* 2013 *Nucl. Fusion* **53** 083007
[20] Jenko F. and Dorland W. 2002 *Phys. Rev. Lett.* **89** 225001
[21] Peterson J. 2011 Relating Gyrokinetic Electron Turbulence to Plasma Confinement in the National Spherical Torus Experiment *PhD Thesis* Princeton University Press, Princeton, NJ 08544

[22] Wang W., Ethier S., Ren Y., Kaye S., Chen J., Startsev E. and Lu Z. 2015 *Nucl. Fusion* **55** 122001
[23] Belova E.V., Gorelenkov N.N., Fredrickson E.D., Tritz K. and Crocker N.A. 2015 *Phys. Rev. Lett.* **115** 015001
[24] Canik J., Guttenfelder W., Maingi R., Osborne T., Kubota S., Ren Y., Bell R., Kugel H., LeBlanc B. and Souhkanovskii V. 2013 *Nucl. Fusion* **53** 113016
[25] Menard J. *et al* 2011 *IEEE/NPSS 24th Symp. on Fusion Engineering (Chicago, IL, USA, 26–30 Jun 2011)* pp 1–8 (http://www.ieee.org/conferences_events/conferences/conferencedetails/index.html?Conf_ID=19303)
[26] Guttenfelder W. *et al* 2013 *Nucl. Fusion* **53** 093022
[27] Told D., Jenko F., Xanthopoulos P., Horton L.D., Wolfrum E. and ASDEX Upgrade Team 2008 *Phys. Plasmas* **15** 102306
[28] Saarelma S., Beurskens M., Dickinson D., Frassinetti L., Leyland M., Roach C. and Contributors E.-J. 2013 *Nucl. Fusion* **53** 123012
[29] Ding S. *et al* 2016 *Nucl. Fusion* **57** 022016
[30] Kaye S., Gerhardt S., Guttenfelder W., Maingi R., Bell R., Diallo A., LeBlanc B. and Podesta M. 2013 *Nucl. Fusion* **53** 063005
[31] Kaye S.M. *et al* 2007 *Phys. Rev. Lett.* **98** 175002
[32] Valovič M. *et al* 2011 *Nucl. Fusion* **51** 073045
[33] IPEG on Confinement, Transport, IPEG on Confinement Modelling, Database, and IPB Editors 1999 *Nucl. Fusion* **39** 2175
[34] Applegate D.J., Roach C.M., Connor J.W., Cowley S.C., Dorland W., Hastie R.J. and Joiner N. 2007 *Plasma Phys. Control. Fusion* **49** 1113
[35] Guttenfelder W., Candy J., Kaye S.M., Nevins W.M., Bell R.E., Hammett G.W., LeBlanc B.P. and Yuh H. 2012 *Phys. Plasmas* **19** 022506
[36] Guttenfelder W. *et al* 2012 *Phys. Plasmas* **19** 056119
[37] Candy J. and Waltz R.E. 2003 *Phys. Rev. Lett.* **91** 045001
[38] Menard J.E. *et al* 2006 *Phys. Rev. Lett.* **97** 095002
[39] Belli E.A. and Candy J. 2010 *Phys. Plasmas* **17** 112314
[40] Guttenfelder W. and Candy J. 2011 *Phys. Plasmas* **18** 022506
[41] Wang W.X., Ethier S., Ren Y., Kaye S., Chen J., Startsev E., Lu Z. and Li Z.Q. 2015 *Phys. Plasmas* **22** 102509
[42] Zhang J., Crocker N.A., Peebles W.A., Carter T.A. and Guttenfelder W. 2013 *Plasma Phys. Control. Fusion* **55** 045011
[43] Wang W.X., Diamond P.H., Hahm T.S., Ethier S., Rewoldt G. and Tang W.M. 2010 *Phys. Plasmas* **17** 072511
[44] Startsev E.A. and Lee W.W. 2014 *Phys. Plasmas* **21** 022505
[45] Kaye S.M., Guttenfelder W., Bell R.E., Gerhardt S.P., LeBlanc B.P. and Maingi R. 2014 *Phys. Plasmas* **21** 082510
[46] Kaye S. *et al* 2015 *Nucl. Fusion* **55** 104002
[47] Wong K.L., Kaye S., Mikkelsen D.R., Krommes J.A., Hill K., Bell R. and LeBlanc B. 2007 *Phys. Rev. Lett.* **99** 135003
[48] Wong K.L., Kaye S., Mikkelsen D.R., Krommes J.A., Hill K., Bell R. and LeBlanc B. 2008 *Phys. Plasmas* **15** 056108
[49] Rechester A.B. and Rosenbluth M.N. 1978 *Phys. Rev. Lett.* **40** 38
[50] Stix T. 1973 *Phys. Rev. Lett.* **30** 833
[51] Smith D.R. *et al* 2009 *Phys. Rev. Lett.* **102** 225005
[52] Smith D.R., Mazzucato E., Lee W., Park H.K., Domier C.W. and Luhmann N.C. 2008 *Rev. Sci. Instrum.* **79** 123501
[53] Ren Y. *et al* 2012 *Phys. Plasmas* **19** 056125
[54] Mazzucato E. *et al* 2009 *Nucl. Fusion* **49** 055001
[55] Mazzucato E. *et al* 2008 *Phys. Rev. Lett.* **101** 075001
[56] Kotschenreuther M., Rewoldt G. and Tang W. 1995 *Comput. Phys. Commun.* **88** 128
[57] Jenko F., Dorland W. and Hammett G.W. 2001 *Phys. Plasmas* **8** 4096
[58] Colyer G.J., Schekochihin A.A., Parra F.I., Roach C.M., Barnes M.A., Ghim Y.C. and Dorland W. 2016 (arXiv:1607.06752)
[59] Ren Y. *et al* 2011 *Phys. Rev. Lett.* **106** 165005
[60] Yuh H.Y. *et al* 2009 *Phys. Plasmas* **16** 056120
[61] Hahm T.S. and Burrell K.H. 1995 *Phys. Plasmas* **2** 1648
[62] Greenwald M. *et al* 1984 *Phys. Rev. Lett.* **53** 352
[63] Balet B. *et al* 1990 *Nucl. Fusion* **30** 2029
[64] Maget P., Garbet X., Geraud A. and Joffrin E. 1999 *Nucl. Fusion* **39** 949
[65] Romanelli M., Bourdelle C. and Dorland W. 2004 *Phys. Plasmas* **11** 3845
[66] Zohm H. 1996 *Plasma Phys. Cont. Fusion* **38** 105
[67] LeBlanc B.P., Bell R.E., Johnson D.W., Hoffman D.E., Long D.C. and Palladino R.W. 2003 *Rev. Sci. Instrum.* **74** 1659
[68] Miller R.L., Chu M.S., Greene J.M., Lin-Liu Y.R. and Waltz R.E. 1998 *Phys. Plasmas* **5** 973
[69] Ruiz Ruiz J. *et al* 2015 *Phys. Plasmas* **22** 122501
[70] Kim E.-J., Holland C. and Diamond P.H. 2003 *Phys. Rev. Lett.* **91** 075003
[71] Parker S.E., Kohut J.J., Chen Y., Lin Z., Hinton F.L. and Lee W.W. 2006 *AIP Conf. Proc.* **871** 193
[72] Levinton F.M. *et al* 2007 *Phys. Plasmas* **14** 056119
[73] Jenko F. 2004 *J. Plasma Fusion Res.* **6** 11
[74] Maeyama S., Idomura Y., Watanabe T.-H., Nakata M., Yagi M., Miyato N., Ishizawa A. and Nunami M. 2015 *Phys. Rev. Lett.* **114** 255002
[75] Howard N., Holland C., White A., Greenwald M. and Candy J. 2016 *Nucl. Fusion* **56** 014004
[76] Wang W.X., Hahm T.S., Lee W.W., Rewoldt G., Manickam J. and Tang W.M. 2007 *Phys. Plasmas* **14** 072306
[77] Idomura Y. 2016 *J. Comput. Phys.* **313** 511
[78] Connor J., Fukuda T., Garbet X., Gormezano C., Mukhovatov V., Wakatani M., The ITB Database Group, The ITPA Topical Group on Transport and Internal Barrier Physics 2004 *Nucl. Fusion* **44** R1
[79] Gormezano C. *et al* 2007 *Nucl. Fusion* **47** S285
[80] Yuh H.Y. *et al* 2011 *Phys. Rev. Lett.* **106** 055003
[81] Dimits A.M. *et al* 2000 *Phys. Plasmas* **7** 969
[82] Peterson J.L., Bell R., Candy J., Guttenfelder W., Hammett G.W., Kaye S.M., LeBlanc B., Mikkelsen D.R., Smith D.R. and Yuh H.Y. 2012 *Phys. Plasmas* **19** 056120
[83] Stutman D., Triz K., Delgado-Aparicio L., Finkenthal M., Kaye S.M., Bell M., Bell R., Kugel H., LeBlanc B. and Yuh H. 2007 *34th European Physical Society Conf. on Plasma Physics (Warsaw, Poland, 2–6 July 2007)* P2.061 (http://iopscience.iop.org/article/10.1088/0741-3335/49/12B/E01/pdf)
[84] Gorelenkov N., Fredrickson E., Belova E., Cheng C., Gates D., Kaye S. and White R. 2003 *Nucl. Fusion* **43** 228
[85] Gorelenkov N.N., Belova E., Berk H.L., Cheng C.Z., Fredrickson E., Heidbrink W.W., Kaye S. and Kramer G.J. 2004 *Phys. Plasmas* **11** 2586
[86] White R.B. and Chance M.S. 1984 *Phys. Fluids* **27** 2455
[87] Tritz K. 2013 private communication
[88] Crocker N. 2016 private communication
[89] Wang W. 2016 private communication
[90] Ren Y. *et al* 2015 *Phys. Plasmas* **22** 110701
[91] Belova E.V., Jardin S.C., Ji H., Yamada M. and Kulsrud R. 2000 *Phys. Plasmas* **7** 4996
[92] Smith D.R., Fonck R.J., McKee G.R. and Thompson D.S. 2012 *Rev. Sci. Instrum.* **83** 10D502
[93] Hillesheim J.C., Dickinson D., Roach C.M., Saarelma S., Scannell R., Kirk A., Crocker N.A., Peebles W.A., Meyer H., and The MAST Team 2016 *Plasma Phys. Control. Fusion* **58** 014020
[94] Lehner T., Rax J.M. and Zou X.L. 1989 *Europhys. Lett.* **8** 759
[95] Vahala L., Vahala G. and Bretz N. 1992 *Phys. Fluids* B **4** 619
[96] Rhodes T.L., Barada K., Peebles W.A. and Crocker N.A. 2016 *Rev. Sci. Instrum.* **87** 11E726
[97] Barada K., Rhodes T.L., Crocker N.A. and Peebles W.A. 2016 *Rev. Sci. Instrum.* **87** 11E601
[98] Tritz K., Clayton D.J., Stutman D. and Finkenthal M. 2012 *Rev. Sci. Instrum.* **83** 10E109